The acoustic Green's function for swirling flow in a lined duct

J.R. Mathews[a,*], N. Peake[a]

[a]*Department of Applied Mathematics and Theoretical Physics, University of Cambridge, Cambridge.*

Abstract

This paper considers the acoustic field inside an annular duct carrying mean axial and swirling flow and with either acoustically hard or lined walls. The particular aim is to compute the Green's function, which is required for predicting the noise generated by known acoustic sources, both approximately and numerically. Asymptotic approximations for first the eigenmodes and then the Green's function are derived in the realistic limit of high reduced frequency, which are found to agree very favourably with results determined numerically, even for relatively modest frequencies. Using a blend of uniform WKB asymptotics and numerics, singular cases in which multiple turning points are present are treated, allowing computation of accurate results across a very wide range of parameter values and flows.

Keywords: Aeroacoustics, turbomachinery, swirl, Green's function, high-frequency asymptotics

1. Introduction

The propagation of acoustic waves through swirling annular duct flow is a crucial issue for the understanding and prediction of sound levels produced by aircraft engines, and therefore for the control of noise pollution around the world's busiest airports. A number of the key technological issues and a discussion of the most important turbomachinery-based noise sources are given in [22].

Noise prediction is often completed using an acoustic analogy. Lighthill [14] famously derived the first acoustic analogy by rearranging the Navier–Stokes equations into a single equation, with the left-hand side being the wave operator in quiescent fluid acting on the density perturbation and the right-hand side being thought of as the sound sources. A formal solution of this equation, assuming that the right hand side is known, is computed as a convolution of the source terms and the Green's function, which in this case is the simple free-space Green's function of the wave operator (see for example Duffy [7]). Lighthill's analogy has been extended in a number of ways, which include considering moving surfaces in the flow, Curle [5] and Ffowcs Williams and Hawkings [8], and choosing a different dependent variable on the left-hand side (for instance, Goldstein [9] and Morfey and Wright [19]). Furthermore, a number of authors have recast Lighthill's analogy to explicitly account for non-trivial base flows by changing the operator on the left-hand side. Lilley [15] extended Lighthill's analogy into a form more suitable for modelling high-speed jet noise by introducing a third-order operator on the left-hand side to represent unidirectional base shear flow. This is often approximated by the linear Pridmore-Brown operator [9], acting on the logarithm of the pressure. In a different direction, Posson and Peake [25] considered an axially sheared and swirling base flow in a duct, and rearranged the governing equations into the form of a (this time) sixth-order linear operator acting on the pressure perturbation. In order to solve this version of the acoustic analogy, the Green's function in ducted swirling flow is therefore clearly required.

It is important to choose a Green's function which is tailored to the geometry, thereby reducing the number of surface terms which need to be calculated in the convolution with the souce terms. For example, for flow in an annular duct the Green's function should have appropriate boundary conditions on the inner

and outer walls. A key first step is then to determine the allowed eigenmodes of the system. The eigenmodes in ducted swirling flow have been considered numerically by a number of authors, including early work by Golubev and Atassi [10] and Tam and Auriault [32]. In Cooper and Peake [4] and Heaton and Peake [11] these eigenmodes were calculated asymptotically in the limit of high frequency, using the WKB method. In Vilenski and Rienstra [33, 34] a lined infinite duct with radially-sheared axial mean flow but with zero swirl is considered, leading to determination of the eigenmodes of the Pridmore–Brown [26] differential equation; both numerical and asymptotic results are presented, with particular focus on the trajectories of the eigenvalues as the wall impedance is varied. In Posson and Peake [23] and Posson and Peake [25] the sixth-order acoustic analogy was derived for a homentropic fluid, and both the eigenmodes and the Green's functions for a hard-walled duct were calculated numerically. A base flow with shear and swirl was considered in a hard-walled infinite duct. In Posson and Peake [24] the results were extended to a duct with acoustically lined walls. In this paper our aim is to extend the above work by finding the Green's function for the acoustic analogy derived in Posson and Peake [25], now using high-frequency asymptotics which we will compare with numerical results.

As we have already noted, the ducted swirling-flow Green's function is required for predicting the noise generated by known source distributions, as performed by Masson et al. [16], Posson and Peake [23, 25]. Alternatively, the Green's function can be used in beamforming to infer information about noise sources and the effectiveness of the lining from acoustic measurements. Significant progress has been made, such as by Sijtsma [30], and beamforming is now one of the major processing tools used to analyse microphone array data in aeroengine noise tests. Inference of source information from far-field data of course requires knowledge of the propagation path from source to observer, which is why the Green's function is required; in practise only relatively simple Green's functions have been used to date, with the most complicated case only assuming radial, piecewise constant axial shear flow in the duct [31]. However, in reality the effects of the swirling flow are significant, and failure to include swirl in the Green's function can potentially lead to spurious source localisation. Application of results from the present paper to beaming in rotor-stator noise tests is therefore a promising line of further inquiry.

This paper is laid out as follows. In Section 2 we present the governing equations for the Green's function together with the boundary conditions in a lined duct, and discuss the swirling base flow. In Section 3 we discuss how to calculate the eigenmodes and the Green's function asymptotically in the high-frequency limit, with the numerical methods described in the Appendix. We analyse the results in Section 4, comparing our asymptotics with numerical results; we will see that the asymptotic eigenmodes and the Green's function are extremely accurate compared to the numerical results, even for very modest frequencies.

2. Acoustic analogy in swirling flow

We will model the aeroengine as an infinite cylindrical duct, although approximations with slowly varying axial ducts have previously been considered by Rienstra [27] and Cooper and Peake [3]. Let the inner and outer duct walls be given by $r^\ddagger = h^\ddagger$ and $r^\ddagger = d^\ddagger$ respectively, where the double dagger $\ddagger$ represents dimensioned coordinates. We non-dimensionalise all distances by $d^\ddagger$, so that the inner wall lies at $r = h := h^\ddagger/d^\ddagger$ and the outer wall at $r = 1$.

In Figure 1 we see the cylindrical coordinate system, with x the axial coordinate, r the radial coordinate and θ the azimuthal coordinate. We let $\underline{u}$, $\underline{v}$ and $\underline{w}$ be the velocities in the x, r and θ directions respectively. We split the inviscid total flow (underlined) into a base flow (subscript 0) plus some small time-harmonic perturbations, so we have

$$(\underline{u}, \underline{v}, \underline{w}, \underline{\rho}, \underline{p}) = (u_0, v_0, w_0, \rho_0, p_0) + (u, v, w, \rho, p), \tag{1}$$

where $\underline{\boldsymbol{u}} = (\underline{u}, \underline{v}, \underline{w})$ is the total velocity of the air, $\underline{\rho}$ is the total density and $\underline{p}$ the total pressure. We non-dimensionalise all velocities by the speed of sound at the outer wall $r^\ddagger = d^\ddagger$, $c_0^\ddagger(d^\ddagger)$. Finally, we non-dimensionalise time by $d^\ddagger/c_0^\ddagger(d^\ddagger)$ and all frequencies by $c_0^\ddagger(d^\ddagger)/d^\ddagger$.
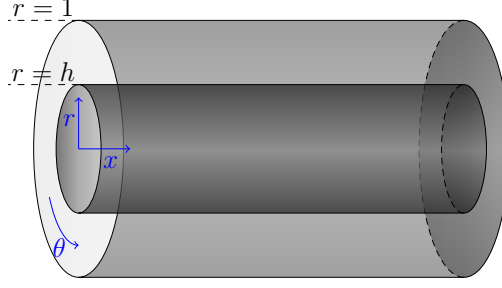
Figure 1: Geometry of the duct.

Our flow will solve the Euler equations;

$$\frac{\partial \underline{\rho}}{\partial t} + \boldsymbol{\nabla} \cdot (\underline{\rho}\underline{\boldsymbol{u}}) = 0, \tag{2}$$

$$\underline{\rho}\left(\frac{\partial \underline{\boldsymbol{u}}}{\partial t} + \underline{\boldsymbol{u}} \cdot \boldsymbol{\nabla}\underline{\boldsymbol{u}}\right) + \boldsymbol{\nabla}\underline{p} = 0. \tag{3}$$

We assume that our fluid is a perfect gas, which gives an energy equation of (amongst many other forms)

$$\frac{\partial \underline{p}}{\partial t} + \underline{\boldsymbol{u}} \cdot \boldsymbol{\nabla}\underline{p} + \gamma\underline{p}(\boldsymbol{\nabla} \cdot \underline{\boldsymbol{u}}) = 0, \tag{4}$$

where γ is the ratio of specific heat capacities ($\gamma = 1.4$ for air). We will assume a homentropic flow so the entropy is constant.

2.1. Acoustic lining of the duct

In the duct we consider the walls to be either hard or to have an acoustic lining. If we consider a duct with hard walls then the boundary conditions become the no-penetration conditions

$$v(h) = v(1) = 0. \tag{5}$$

To mathematically model the acoustic lining we introduce the impedances $Z_h, Z_1 \in \mathbb{C}$ of the liner at the duct walls. We non-dimensionalise the impedances by $Z_j = Z_j^\ddagger \rho_0^\ddagger(d^\ddagger)c_0^\ddagger(d^\ddagger)$, and assume that these impedances are uniform. The boundary conditions for the unsteady flow are then the standard Myers [20] boundary conditions (allowing for slip flow at the duct walls)

$$\begin{aligned}
\mathrm{i}\omega v &= \left(-\mathrm{i}\omega + u_0\frac{\partial}{\partial x} + \frac{w_0}{r}\frac{\partial}{\partial \theta}\right)\left(\frac{p}{Z_h}\right) \quad \text{on } r = h, \\
-\mathrm{i}\omega v &= \left(-\mathrm{i}\omega + u_0\frac{\partial}{\partial x} + \frac{w_0}{r}\frac{\partial}{\partial \theta}\right)\left(\frac{p}{Z_1}\right) \quad \text{on } r = 1.
\end{aligned} \tag{6}$$

Here and throughout we assume the time dependence of the flow is of the form $\exp(-\mathrm{i}\omega t)$. The impedances we choose are of the form $Z_j = 1 - Z_{\mathrm{imag}}\mathrm{i}$, where $\mathrm{Re}(Z_j)$ is positive in order to ensure that the lining absorbs energy and is therefore physically realistic. A typical choice we use for the impedance is $Z_j = 1 - 2\mathrm{i}$. To get more realistic values of impedance (in a hollow duct with no flow) we could use the Cremer optimum value [29]. This gives $Z_j = \omega K_n$, where K_n is calculated in Rienstra [29], and for $n = 0$ we find $K_0 = 0.28 - 0.12i\mathrm{i}$. The case of hard walls corresponds to an impedance of $Z_j = \infty$, for which the boundary conditions in Eq. (6) reduce to Eq. (5).

2.2. Swirling base flow

The swirling base flow is a solution of the Euler equations, which we define by specifying the base flow velocities, and then calculate the pressure, density and speed of sound. We choose a base flow of the form

$$(u_0, v_0, w_0) = (U_x(r), 0, U_\theta(r)), \tag{7}$$

where $U_x(r)$ and $U_\theta(r)$ are freely chosen. This will give a base flow representative of swirling mean flow between the rotor and stator in an aeroengine. Numerical CFD (Computational Fluid Dynamics) calculations suggest that for the swirling flow between the rotor and stator, u_0 and w_0 have a similar amplitude, while the amplitude of v_0 is around $10 - 15\%$ of u_0 and w_0. Thus, neglecting the radial mean flow should give reasonable results, although the gradients of the radial mean flow v_0 could be a comparable size to u_0 and w_0 and therefore still play a role in sound propagation. The assumption that the base flow velocity only depends on r is needed to simplify calculations, but again in CFD results the dependence of θ and x is considerably weaker than the dependence on r. The speed of sound c_0 is given by

$$c_0^2(r) = c_0^2(1) + (\gamma - 1) \int_1^r \frac{U_\theta^2(s)}{s} ds. \tag{8}$$

The density is given by

$$\rho_0(r) = [c_0^2(r)]^{1/(\gamma-1)}, \tag{9}$$

and finally the pressure is given by

$$p_0(r) = p_0(1) - \int_r^1 \frac{\rho_0(s)U_\theta^2(s)}{s} ds. \tag{10}$$

2.3. Acoustic analogy

In Posson and Peake [25] an acoustic analogy was derived for the pressure perturbation. The analogy was derived by considering an exact rearrangement of the Euler equations, such that we got a single, sixth-order linear differential equation for pressure on the left-hand side. On the right-hand side is a source term $\mathbb{S}$ which includes the non-linear effects, viscosity effects and the rotor-stator geometry. The analogy is given by

$$\mathcal{F}(p) = \mathbb{S}, \tag{11}$$

where the differential operator $\mathcal{F}$ is (using the notation from Mathews [17])

$$\mathcal{F} = \left(\frac{1}{c_0^2} \frac{D_0{}^2}{Dt^2} - \frac{\partial^2}{\partial x^2} - \frac{1}{r^2} \frac{\partial^2}{\partial \theta^2} \right) \mathcal{R}^2 + \left(\frac{1}{r} \frac{D_0}{Dt} - U_x' \frac{\partial}{\partial x} - \left(\frac{U_\theta}{r^2} + \frac{U_\theta'}{r} \right) \frac{\partial}{\partial \theta} \right) \mathcal{R}\mathcal{T} \tag{12}$$

$$+ \mathcal{R} \frac{D_0}{Dt} \frac{\partial}{\partial r} \mathcal{T} - \frac{D_0}{Dt} \left[2U_x' \frac{\partial}{\partial x} \frac{D_0}{Dt} + 2 \left(\frac{U_\theta}{r} \right)' \frac{\partial}{\partial \theta} \frac{D_0}{Dt} + \mathcal{U}_\theta' \right] \mathcal{T},$$

where

$$\mathcal{R} = \frac{D_0{}^2}{Dt^2} + \mathcal{U}_\theta, \quad \mathcal{T} = -\frac{D_0}{Dt} \frac{\partial}{\partial r} - \frac{2U_\theta}{r^2} \frac{\partial}{\partial \theta} + \frac{U_\theta^2}{rc_0^2} \frac{D_0}{Dt}, \quad \frac{D_0}{Dt} = \frac{\partial}{\partial t} + U_x \frac{\partial}{\partial x} + \frac{U_\theta}{r} \frac{\partial}{\partial \theta}, \tag{13}$$

and

$$\mathcal{U}_\theta(r) = \frac{2U_\theta(r)}{r} \left(\frac{U_\theta(r)}{r} + U_\theta'(r) \right). \tag{14}$$

The source term $\mathbb{S}$ is given in Posson and Peake [25], and need not be stated here.

3. High-frequency analytic Green's function

In this paper we aim to find the reduced Green's function $G_\omega(\boldsymbol{x}|\boldsymbol{x}_0)$ of Eq. (12), which satisfies

$$\mathcal{F}\left(G_\omega(\boldsymbol{x}|\boldsymbol{x}_0)\mathrm{e}^{-\mathrm{i}\omega t}\right) = \delta(\boldsymbol{x}-\boldsymbol{x}_0)\mathrm{e}^{-\mathrm{i}\omega t} = \delta(x-x_0)\frac{\delta(r-r_0)}{r}\delta(\theta-\theta_0)\mathrm{e}^{-\mathrm{i}\omega t}, \tag{15}$$

of the form

$$G_\omega(\boldsymbol{x}|\boldsymbol{x}_0) = \frac{1}{4\pi^2}\sum_{n=-\infty}^{\infty}\mathrm{e}^{\mathrm{i}n(\theta-\theta_0)}\int_{\mathbb{R}}G_n(r|r_0;\omega,k)\mathrm{e}^{\mathrm{i}k(x-x_0)}\mathrm{d}k, \tag{16}$$

where we choose a circumferential Fourier series to ensure periodicity. Using standard results from Bender and Orszag [1] gives G_n as

$$G_n(r|r_0;\omega,k) = \frac{1}{r_0\mathcal{W}(r_0,k)J(r_0,k)}\begin{cases}g_1(r_0;k)g_2(r;k) & r \le r_0 \\ g_2(r_0;k)g_1(r;k) & r > r_0\end{cases}, \tag{17}$$

where $\mathcal{W}(r_0,k)$ is the Wrońskian of $g_1(r;k)$ and $g_2(r;k)$. The functions $g_1(r;k)$ and $g_2(r;k)$ solve the second order ordinary differential equation

$$\frac{p_0}{c_0^2 r}(\mathcal{U}_\theta - \Omega^2)^2\Omega^2\frac{\mathrm{d}}{\mathrm{d}r}\left(\frac{rc_0^2}{p_0(\Omega^2 - \mathcal{U}_\theta)}\frac{\mathrm{d}g_j}{\mathrm{d}r}\right) + \left[(\mathcal{U}_\theta - \Omega^2)^2\left(\frac{\Omega^2}{c_0^2} - k^2 - \frac{n^2}{r^2}\right)\right. \tag{18}$$

$$\left. + \Upsilon(\mathcal{U}_\theta - \Omega^2)\left[\Upsilon + \Omega\left(\frac{1}{r} - \frac{\rho_0'}{\rho_0}\right)\right] - \Upsilon'\Omega(\Omega^2 - \mathcal{U}_\theta) + \Upsilon[\Omega(\Omega^2 - \mathcal{U}_\theta)]'\right]g_j = 0,$$

with $g_1(r;k)$ satisfying the Myers boundary condition at $r = 1$ and $g_2(r;k)$ satisfying the Myers boundary condition at $r = h$. Note that the primes in Eq. (18) denote differentiation with respect to r. The functions Ω and Υ are given by

$$\Omega(r,k) = \omega - kU_x(r) - \frac{nU_\theta(r)}{r} \text{ and } \Upsilon(r,k) = \frac{U_\theta^2(r)}{rc_0^2(r)}\Omega(r,k) + \frac{2nU_\theta(r)}{r^2}, \tag{19}$$

while the function J arises from the jump in the derivative of $g_j(r;k)$ at $r = r_0$, and is given by

$$J(r_0,k) = [\Omega^2(r_0,k) - \mathcal{U}_\theta(r_0)]\Omega^2(r_0,k). \tag{20}$$

From the derivation of the acoustic analogy in Posson and Peake [25] we have $\rho_0\mathcal{R}(v) = \mathcal{T}(p)$ when we ignore source terms. Inserting this into the Myers boundary conditions in Eq. (6) and Fourier transforming gives the boundary condition at $r = h$ for $g_2(r;k)$ as

$$\frac{\mathrm{d}g_2}{\mathrm{d}r}(h;k) - \left[\frac{2nU_\theta(h)}{h^2\Omega(h;k)} + \frac{U_\theta^2(h)}{hc_0^2(h)}\right]g_2(h;k) + \frac{\mathrm{i}\rho_0(h)}{\omega Z_h}\left[\Omega^2(h;k) - \mathcal{U}_\theta(h)\right]g_2(h;k) = 0, \tag{21}$$

while the boundary condition at $r = 1$ for $g_1(r;k)$ is given by

$$\frac{\mathrm{d}g_1}{\mathrm{d}r}(1;k) - \left[\frac{2nU_\theta(1)}{\Omega(1;k)} + \frac{U_\theta^2(1)}{c_0^2(1)}\right]g_1(1;k) - \frac{\mathrm{i}\rho_0(1)}{\omega Z_1}\left[\Omega^2(1;k) - \mathcal{U}_\theta(1)\right]g_1(1;k) = 0. \tag{22}$$

If we let $Z_j \to \infty$ then the final terms in Eq. (21) and Eq. (22) become zero and we recover the hard wall boundary conditions from Posson and Peake [25].

5

3.1. High frequency limit

The differential equation in Eq. (18) is much too complicated to find an exact analytical solution. Instead, we consider the equation in the high-frequency limit ($\omega \to \infty$), which allows us to use the WKB method to find an approximate solution. We introduce a scaling of the axial wavenumber and azimuthal number with frequency;

$$\kappa = \frac{k}{\omega} \text{ and } \eta = \frac{n}{\omega}, \tag{23}$$

and assume that both $\kappa, \eta = \mathcal{O}(1)$. We also introduce the scaled function $\Phi(r,k)$ and $\Upsilon^*(r,k)$ such that $\Omega = \omega\Phi$ and $\Upsilon = \omega\Upsilon^*$.

We then consider the differential equation with the new scalings, which is given by Eq. (B.2). When ω is large, some of the terms in the differential equation can be discarded. We assume that $\Phi = \mathcal{O}(1)$ and make the change of variable

$$g_j(r;\kappa) = \frac{\rho_0^{1/2}(r)\Phi(r,\kappa)\mathcal{P}_j(r;\kappa)}{r^{1/2}}, \tag{24}$$

and then to leading order the differential equation becomes

$$\mathcal{P}_j''(r;\kappa) + \omega^2 q_n(r,\kappa)\mathcal{P}_j(r;\kappa) = 0 \text{ where } q_n(r,\kappa) = \left(\frac{\Phi^2(r,\kappa)}{c_0^2(r)} - \kappa^2 - \frac{\eta^2}{r^2} \right). \tag{25}$$

We can then use the WKB method to find solutions of this equation. We only consider the physical optics approximation [1]. The form of $\mathcal{P}_j(r;\kappa)$ depends on how many zeros $q_n(r,\kappa)$ has in the duct or close to it in the complex r plane. When $q_n(r,\kappa)$ has no zeros close to the duct then $\mathcal{P}_j(r;\kappa)$ is a linear combination of exponentials, given by

$$\mathcal{P}_j(r;\kappa) = (q_n(r,\kappa))^{-1/4} \left(A^j(\kappa)\mathrm{e}^{i\omega\psi_n(r,\kappa)} + B^j(\kappa)\mathrm{e}^{-i\omega\psi_n(r,\kappa)} \right), \tag{26}$$

with

$$\psi_n(r,\kappa) = \int_h^r \sqrt{q_n(s,\kappa)}\mathrm{d}s, \tag{27}$$

for some constants A^j and B^j. If $q_n(r,\kappa)$ has a single zero (at $r = r_c$ say) we use the uniformly-valid Langer solution [1, 11, 13] which gives

$$\mathcal{P}_j(r;\kappa) = \sqrt{\pi} \left(\frac{\tau(r,\kappa)}{q_n(r,\kappa)} \right)^{1/4} \left[A^j(\kappa)\,\mathrm{Ai}\,(-\tau(r,\kappa)) + B^j(\kappa)\,\mathrm{Bi}\,(-\tau(r,\kappa)) \right], \tag{28}$$

where

$$\tau(r,\kappa) = \left(\frac{3\omega\Psi_n(r,\kappa)}{2} \right)^{2/3} \text{ and } \Psi_n(r,\kappa) = \int_{r_c}^r \sqrt{q_n(s,\kappa)}\mathrm{d}s. \tag{29}$$

For a given value of κ, we define the square root in Eq. (29) to have a branch cut on the positive or negative imaginary axis. We consider $q_n(r,\kappa)$ for $h \leq r \leq 1$, and choose the branch cut to be the imaginary axis we do not cross, and we can choose either imaginary axis if we cross neither. The branch cuts of the other roots (2/3 and 1/4) are similarly chosen to avoid crossing any branch cuts as r varies in the duct.

If $q_n(r,\kappa)$ has more than a single zero we will find the solution of the differential equation Eq. (25) numerically, as shown in Section 3.3. In our change of variables, the Green's function G_n is now given by

$$G_n(r|r_0;\kappa) = \left(\frac{\rho_0(r)r_0}{\rho_0(r_0)r} \right)^{1/2} \frac{\Phi(r,\kappa)}{r_0\mathcal{V}(r_0,\kappa)J(r_0,\kappa)\Phi(r_0,\kappa)} \begin{cases} \mathcal{P}_1(r_0;\kappa)\mathcal{P}_2(r;\kappa) & r \leq r_0 \\ \mathcal{P}_2(r_0;\kappa)\mathcal{P}_1(r;\kappa) & r > r_0 \end{cases}, \tag{30}$$

where the Wrońskian $\mathcal{V}(r_0,\kappa)$ is now independent of r_0 by Abel's theorem [2]. The boundary conditions after the change of variables become

$$\frac{\mathrm{d}\mathcal{P}_2}{\mathrm{d}r}(h;\kappa) + f_2(h,\kappa)\mathcal{P}_2(h;\kappa) = 0 \text{ and } \frac{\mathrm{d}\mathcal{P}_1}{\mathrm{d}r}(1;\kappa) + f_1(1,\kappa)\mathcal{P}_1(1;\kappa) = 0, \tag{31}$$

6

where $f_1(1, \kappa)$ and $f_2(h, \kappa)$ can easily be determined from Eq. (21) and Eq. (22). For a given κ, these boundary conditions will then determine the solutions $\mathcal{P}_j(r; \kappa)$ up to a constant. To determine the values of κ that are eigenmodes, we look for a solution $\mathcal{P}(r; \kappa)$ that solves both boundary conditions in Eq. (31), or equivalently κ that solves $\mathcal{V}(r_0, \kappa) = 0$.

3.1.1. Applicability of high frequency limit

The high-frequency limit in Eq. (25) is only valid when $\Phi = \mathcal{O}(1)$. Thus, near the critical layer, where $\Phi(r, \kappa)$ is close to zero, the high-frequency limit will not be valid since the coefficient of the second derivative in Eq. (B.2) approaches zero. Let us consider the Wrońskian $\mathcal{W}(r_0, k)$ of the two solutions to the differential equation in Eq. (25) which satisfy the Myers boundary conditions. Solving the dispersion relation $\mathcal{W} = 0$ should give us all the eigenmodes of the flow. However, since the high-frequency limit is not applicable near the critical layer, we will not be able to find the hydrodynamic modes, and we will only find the acoustic eigenmodes from solving $\mathcal{W} = 0$. If we were instead to look at solutions of $\mathcal{W} = 0$ for the full differential equation then we would find both the acoustic and hydrodynamic eigenmodes. An analytic description of the hydrodynamic modes is given in Heaton and Peake [12].

3.1.2. Regions for WKB method

We define the region of r space where we use the one turning point solution to consist of the r_c which lie within a distance of $\mathcal{O}(\omega^{-2/3})$ from the duct $[h, 1]$ in the complex plane. The region is defined from the classical WKB method [1], and is the region where we use the Airy function solution. We denote this region $\mathscr{R}$, with

$$\mathscr{R} = \left\{ r \in \mathbb{C} \,\middle|\, |r - r_1| < \omega^{-2/3} \text{ for } r_1 \in [h, 1] \right\}, \tag{32}$$

although since the distance to the duct only has to be $\mathcal{O}(\omega^{-2/3})$, we can choose other values of the exponent of ω in Eq. (32). We see an example in Figure 2a. We use the one turning point solution in $\mathscr{R}$, and the zero turning point solution in $\mathbb{C} \backslash \mathscr{R}$ as well. We could also use the one turning point solution in $\mathbb{C} \backslash \mathscr{R}$, but using the asymptotic behaviour of the Airy functions reduces the solution to the same form as the zero turning point solution.

We next find the region of κ space where we use the one turning point solution. We use the definition of $q_n(r, \kappa)$ from Eq. (25) and solve $q_n(r, \kappa) = 0$ for $r \in \mathscr{R}$, which gives a quadratic equation in κ. Thus, we find that $\kappa = s^\pm(r)$, where

$$s^\pm(r) = \frac{U_x(r) \left(1 - \frac{\eta U_\theta(r)}{r}\right) \pm c_0(r) \sqrt{\left(1 - \frac{\eta U_\theta(r)}{r}\right)^2 + \frac{\eta^2}{r^2} [U_x^2(r) - c_0^2(r)]}}{U_x^2(r) - c_0^2(r)}. \tag{33}$$

We denote the region of κ space where we use the one turning point solution as $\mathscr{K}$, and it is given by $\mathscr{K} = s^+(\mathscr{R}) \cup s^-(\mathscr{R})$. In this region there is either a critical point r_c in the duct, or a critical point close enough to the duct that we should use the one turning point solution. Some examples of $\mathscr{K}$ regions are given in Figure 2, although we have plotted $\omega \mathscr{K}$ to show the regions in the k complex plane rather than the κ complex plane. We find that there are three distinct shapes that the region $\mathscr{K}$ takes. Type 1 corresponds to $q_n(r, \kappa)$ having no solutions $\kappa \in \mathbb{R}$ for $r \in [h, 1]$. Type 2 corresponds to $q_n(r, \kappa)$ having solutions $\kappa \in \mathbb{R}$ for some values of $r \in [h, 1]$, while type 3 corresponds to $q_n(r, \kappa)$ having solutions $\kappa \in \mathbb{R}$ for all values of $r \in [h, 1]$.

In Figure 2 we see the three different regimes for the flow $U_x = 0.5$, $U_\theta(r) = 0.1r + 0.1/r$, which is the flow we consider in Section 4.1. If we have non-zero swirl then the $\mathscr{K}$ region does not have left-right symmetry, although it is still symmetric about the real line. The lining has no effect on the region $\mathscr{K}$. The different regimes for $\mathscr{K}$ have no effect on the method for determining the Green's function or eigenmodes. However, the regime generally changes the number of cut-on eigenmodes, since we find most (but not all) of the cut-on modes in the region $\mathscr{K}$.
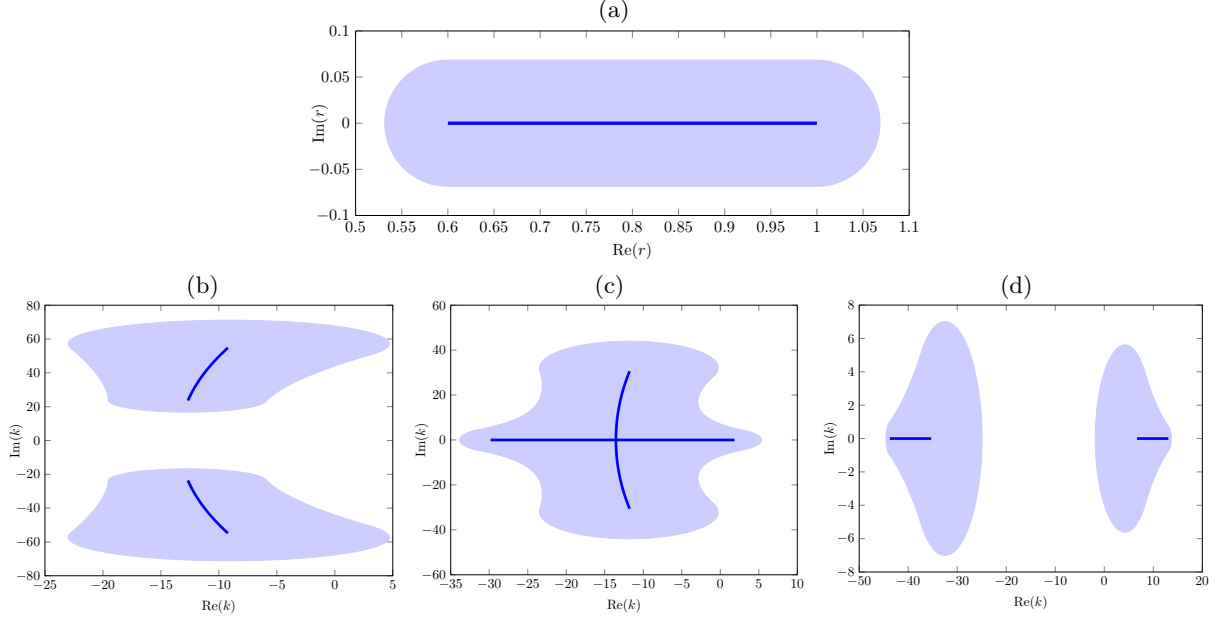
Figure 2: (a) Region $\mathscr{R}$ when $\omega = 25$, $h = 0.6$; (b) to (d) three different regimes for the region $\omega\mathscr{K}$ when $h = 0.6$, $\omega = 25$, $U_x = 0.5$ and $U_\theta(r) = 0.1r + 0.1/r$. (b) $n = 30$ (Type 1); (c) $n = 20$ (Type 2); (d) $n = 10$ (Type 3). Blue line: exact turning points; shaded region: close to a turning point.

3.2. Asymptotic dispersion relations for eigenmodes

Let us first define $r_2 = h$ and $r_1 = 1$. At the duct walls we find that

$$\mathcal{P}_j(r_j; \kappa) = A^j(\kappa)\mathscr{A}^j(\kappa) + B^j(\kappa)\mathscr{B}^j(\kappa), \tag{34}$$

with

$$\mathscr{A}^j(\kappa) = \frac{1}{1+\mathrm{i}}(q_j(\kappa))^{-1/4}\mathrm{e}^{\mathrm{i}\omega\psi_j(\kappa)}\mathbb{1}_{\mathscr{K}^C} + \sqrt{\pi}\left[\left(\frac{\tau_j(\kappa)}{q_j(\kappa)}\right)^{1/4}\mathrm{Ai}\left(-\tau_j(\kappa)\right)\right]\mathbb{1}_{\mathscr{K}}, \tag{35}$$

and

$$\mathscr{B}^j(\kappa) = \frac{1}{1+\mathrm{i}}(q_j(\kappa))^{-1/4}\mathrm{e}^{-\mathrm{i}\omega\psi_j(\kappa)}\mathbb{1}_{\mathscr{K}^C} + \sqrt{\pi}\left[\left(\frac{\tau_j(\kappa)}{q_j(\kappa)}\right)^{1/4}\mathrm{Bi}\left(-\tau_j(\kappa)\right)\right]\mathbb{1}_{\mathscr{K}}, \tag{36}$$

where $\tau_j(\kappa) = \tau(r_j, \kappa)$, $q_j(\kappa) = q_n(r_j, \kappa)$, $\psi_j(\kappa) = \psi_n(r_j, \kappa)$ and $\mathbb{1}_{\mathscr{K}}$ is the indicator function. We have scaled the zero turning point solution so that the Wrońskian is constant for all values of κ. We also calculate that

$$\frac{\mathrm{d}\mathcal{P}_j}{\mathrm{d}r}(r_j; \kappa) = A^j(\kappa)\mathbb{A}^j(\kappa) + B^j(\kappa)\mathbb{B}^j(\kappa), \tag{37}$$

where

$$\mathbb{A}^j(\kappa) = \frac{1}{1+\mathrm{i}}\left(-\frac{\frac{\partial}{\partial r}q_j(\kappa)}{4q_j(\kappa)} + \mathrm{i}\omega\sqrt{q_j(\kappa)}\right)(q_j(\kappa))^{-1/4}\mathrm{e}^{\mathrm{i}\omega\psi_j(\kappa)}\mathbb{1}_{\mathscr{K}^C} + \sqrt{\pi}\left(\frac{\tau_j(\kappa)}{q_j(\kappa)}\right)^{1/4} \tag{38}$$

$$\times\left[\left(\frac{1}{6}\frac{\frac{\partial}{\partial r}\Psi_j(\kappa)}{\Psi_j(\kappa)} - \frac{1}{4}\frac{\frac{\partial}{\partial r}q_j(\kappa)}{q_j(\kappa)}\right)\mathrm{Ai}(-\tau_j(\kappa)) - \frac{2}{3}\frac{\frac{\partial}{\partial r}\Psi_j(\kappa)}{\Psi_j(\kappa)}\tau_j(\kappa)\mathrm{Ai}'(-(\tau_j(\kappa)))\right]\mathbb{1}_{\mathscr{K}},$$

8

and

$$\mathbb{B}^j(\kappa) = \frac{1}{1+\mathrm{i}}\left(-\frac{\frac{\partial}{\partial r}q_j(\kappa)}{4q_j(\kappa)}-\mathrm{i}\omega\sqrt{q_j(\kappa)}\right)(q_j(\kappa))^{-1/4}\mathrm{e}^{-\mathrm{i}\omega\psi_j(\kappa)}\mathbb{1}_{\mathscr{K}^C} + \sqrt{\pi}\left(\frac{\tau_j(\kappa)}{q_j(\kappa)}\right)^{1/4} \tag{39}$$

$$\times\left[\left(\frac{1}{6}\frac{\frac{\partial}{\partial r}\Psi_j(\kappa)}{\Psi_j(\kappa)}-\frac{1}{4}\frac{\frac{\partial}{\partial r}q_j(\kappa)}{q_j(\kappa)}\right)\mathrm{Bi}(-\tau_j(\kappa))-\frac{2}{3}\frac{\frac{\partial}{\partial r}\Psi_j(\kappa)}{\Psi_j(\kappa)}\tau_j(\kappa)\,\mathrm{Bi}'(-(\tau_j(\kappa)))\right]\mathbb{1}_{\mathscr{K}}.$$

Setting $A^j(\kappa) = 1$ and applying the boundary conditions in Eq. (31) gives

$$B^2(\kappa)\left(\mathbb{B}^2(\kappa)+f_2(h,\kappa)\mathscr{B}^2(\kappa)\right)=-\mathbb{A}^2(\kappa)-f_2(h,\kappa)\mathscr{A}^2(\kappa), \tag{40}$$

and

$$B^1(\kappa)\left(\mathbb{B}^1(\kappa)+f_1(1,\kappa)\mathscr{B}^1(\kappa)\right)=-\mathbb{A}^1(\kappa)-f_1(1,\kappa)\mathscr{A}^1(\kappa), \tag{41}$$

which we solve to find $B^1(\kappa)$ and $B^2(\kappa)$. We then calculate that the Wrońskian is given by $\mathcal{V}(\kappa) = \omega\left[B^1(\kappa)-B^2(\kappa)\right]$, so the dispersion relation is

$$\mathcal{V}(\kappa)=\omega\left[B^1(\kappa)-B^2(\kappa)\right]=0, \tag{42}$$

which we solve to find the asymptotic eigenmodes.

To solve the dispersion relation in Eq. (42) we employ numerical methods. Our main approach is to use the numerical eigenmodes as a starting guess and then use a numerical non-linear equation solver, for example "fsolve" in MATLAB. Previously, there have been attempts to solve simpler dispersion relations asymptotically. Although Heaton and Peake [11] give an asymptotic method to solve their dispersion relation, it is only valid for far away cut-off modes. In Vilenski and Rienstra [33], more terms were calculated in the asymptotic method. However, their results do not include swirl and rely on the impedances Z_j being large, so are not universally applicable. In addition, their results only apply when there are no zeros of $q_n(r,\kappa)$, so for $\kappa \in \mathbb{C}\backslash\mathscr{K}$.

3.3. Two turning points

Our method in the previous subsection to find the eigenmodes is only applicable when $q_n(r,\kappa)$ had at most a single zero close to the duct. There is no simple analogue to the uniformly-valid Langer solution when $q_n(r,\kappa)$ has two or more zeros; a uniformly-valid solution can be found using parabolic cylinder functions [21], but it is difficult to implement.

Instead we look for numerical solutions to the differential equation in the high frequency limit, given by Eq. (25). When we solved Eq. (25) for $\mathcal{P}_j(r;\kappa)$ with $q_n(r,\kappa)$ having a single zero we found the null space was essentially spanned by the Airy functions $\mathrm{Ai}(-\tau(r,\kappa))$ and $\mathrm{Bi}(-\tau(r,\kappa))$. We now find the null space of the differential equation Eq. (25) numerically using the null space command in Chebfun [6] for each κ, giving functions $\varphi_1(r;\kappa)$ and $\varphi_2(r;\kappa)$, so that the general solution of the differential equation is given by $\mathcal{P}_j(r,\kappa) = A\varphi_1(r;\kappa)+B\varphi_2(r;\kappa)$.

To find the eigenmodes we define $\mathscr{A}^j(\kappa)=\varphi_1(j,\kappa)$, $\mathscr{B}^j(\kappa)=\varphi_2(j,\kappa)$, $\mathbb{A}^j(\kappa)=\varphi_1'(j;\kappa)$ and $\mathbb{B}^j(\kappa)=\varphi_2'(j;\kappa)$. We then apply the boundary conditions as in Section 3.2, setting $A^j(\kappa)=1$ and calculating $B^j(\kappa)$ as in Eq. (40) and Eq. (41). However, the Wrońskian $\mathcal{V}$ is slightly different and is now given by

$$\mathcal{V}(\kappa)=\left[B^1(\kappa)-B^2(\kappa)\right]\left(\varphi_1(r_0;\kappa)\varphi_2'(r_0;\kappa)-\varphi_1'(r_0;\kappa)\varphi_2(r_0;\kappa)\right). \tag{43}$$

The second part of the Wrońskian is a now an unknown constant independent of r. We have now shown how to determine the eigenmodes of our swirling flow, and in the next section we move on to determining the Green's function itself.

9

3.4. Evaluating the Green's function

Instead of finding G_ω in Eq. (16) we calculate $\widehat{p}_\omega$, which is defined by

$$\widehat{p}_\omega(\boldsymbol{x}|\boldsymbol{x}_0) = \frac{1}{4\pi^2} \sum_{n=-\infty}^{\infty} \mathrm{e}^{in(\theta-\theta_0)} \int_{\mathbb{R}} \widehat{p}_n(r|r_0;\omega,k)\mathrm{e}^{ik(x-x_0)}\mathrm{d}k, \qquad (44)$$

where

$$\widehat{p}_n(r|r_0;\omega,k) = \frac{1}{2\pi r_0 \mathcal{W}(r_0,k)} \begin{cases} g_1(r_0;k)g_2(r;k) & r \leq r_0 \\ g_2(r_0;k)g_1(r;k) & r > r_0 \end{cases}, \qquad (45)$$

so $\widehat{p}_n$ and G_n differ by a factor of $J(r_0,k)/2\pi$. The factor of $1/2\pi$ ensures that our definition of $\widehat{p}_\omega$ matches the definition in Posson and Peake [25]. The pressure now satisfies

$$\frac{1}{2\pi}\frac{D_0^2}{Dt^2}\mathcal{R}(p) = \int \widehat{p}_\omega(r,x,\theta|r_0,x_0,\theta_0)\mathbb{S}(r_0,x_0,\theta_0)\mathrm{d}\boldsymbol{x}_0\mathrm{e}^{-i\omega t}, \qquad (46)$$

since

$$\mathcal{F}\left(\widehat{p}_\omega \mathrm{e}^{-i\omega t}\right) = \frac{1}{2\pi}\frac{D_0^2}{Dt^2}\mathcal{R}\left(\delta(\boldsymbol{x}-\boldsymbol{x}_0)\mathrm{e}^{-i\omega t}\right). \qquad (47)$$

We consider the Green's function $\widehat{p}_\omega$ rather than G_ω for two reasons. Firstly, it allows easy comparison with the case of no swirl and uniform axial flow, which was considered in Rienstra and Tester [28]. In the case of no swirl and uniform axial flow, the right-hand side of Eq. (47) is the fourth power of the material derivative acting on the Dirac delta. The operator $\mathcal{F}$ is given by the fourth power of the material derivative acting on the convected wave equation, so we just have to find the Green's function of the convected wave equation. Secondly, $\widehat{p}_\omega$ would be more useful when calculating the pressure using the sources terms from Posson and Peake [25]. This is because we apply the derivatives from the source terms to the Green's function using integration by parts. When we Fourier transform, these derivatives become multiplication by a function such as J.

To calculate $\widehat{p}_\omega$ we find the inverse Fourier transform of $\widehat{p}_n$, which is given by

$$\int_{\mathbb{R}} \widehat{p}_n(r|r_0;\omega,k)\mathrm{e}^{ik(x-x_0)}\mathrm{d}k = \int_{\Gamma} [g_1(r_0;k)g_2(r;k)\mathbb{1}_{r\leq r_0} + g_2(r_0;k)g_1(r;k)\mathbb{1}_{r>r_0}]\frac{\mathrm{e}^{ik(x-x_0)}}{2\pi r_0 \mathcal{W}(r_0,k)}\mathrm{d}k, \qquad (48)$$

where Γ is given in Figure 3a, and is determined by causality considerations. This procedure involves considering the eigenmodes when the frequency has a small (positive) imaginary part, in which case the eigenmodes and critical layer lie off the real axis and Γ is just the real line. As we take the limit of the imaginary part to zero, we get the contour in Figure 3a. To perform the integration we close the contour in the upper or lower half plane depending on whether $x > x_0$ or $x < x_0$. When $x > x_0$ we close the contour
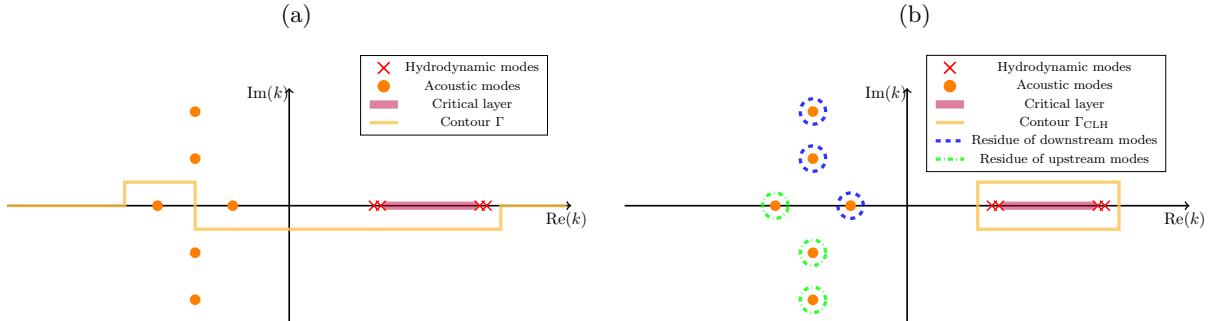

Figure 3: Schematic of eigenmodes and integration contour. (a) Original contour Γ; (b) contour Γ_{CLH} and residues. We also see acoustic modes (orange circles), hydrodynamic modes (red crosses), critical layer (solid pink line), residues of the downstream eigenmodes (blue, dashed) and residue of the upstream eigenmodes (green, dot-dashed).

in the upper half plane, and the Green's function is equal to the sum of the residues at the downstream acoustic eigenmodes, plus a critical layer contribution, which we describe in Section 3.6. When $x < x_0$ we close the contour in the lower half plane, and get a sum of the residues at the upstream acoustic eigenmodes, with no contribution from the critical layer.

3.5. Contribution from acoustic eigenmodes

The total contribution to $\widehat{p}_\omega$ from the acoustic eigenmodes is given by

$$\widehat{p}_\omega^A(\boldsymbol{x}|\boldsymbol{x}_0) = \sum_{n=-\infty}^{\infty} \mathrm{e}^{\mathrm{i}n(\theta-\theta_0)} \sum_{\mathcal{K}_n^{\pm}} \widehat{p}_n^m(x,r|x_0,r_0), \tag{49}$$

where

$$\widehat{p}_n^m(x,r|x_0,r_0) = \pm\frac{2\pi\mathrm{i}}{4\pi^2} \operatorname{Res}\{\widehat{p}_n(r|r_0;\omega,k)\mathrm{e}^{\mathrm{i}k(x-x_0)}, k = k_n^m\}. \tag{50}$$

The $\pm$ comes from whether $x > x_0$ or $x < x_0$, with $\mathcal{K}_n^+$ consisting of all downstream acoustic modes and $\mathcal{K}_n^-$ consisting of all upstream acoustic modes. We calculate that

$$\widehat{p}_n^m(x,r|x_0,r_0) = \pm\frac{\mathrm{i}\omega}{4\pi^2} \left(\frac{\rho_0(r)r_0}{\rho_0(r_0)r}\right)^{1/2} \frac{\Phi(r,\kappa_n^m)\mathrm{e}^{\mathrm{i}\omega\kappa_n^m(x-x_0)}}{r_0\frac{\partial\mathcal{V}}{\partial\kappa}(\kappa_n^m)\Phi(r_0,\kappa_n^m)} \begin{cases} \mathcal{P}_1(r_0;\kappa_n^m)\mathcal{P}_2(r;\kappa_n^m) & r \leq r_0 \\ \mathcal{P}_2(r_0;\kappa_n^m)\mathcal{P}_1(r;\kappa_n^m) & r > r_0 \end{cases}. \tag{51}$$

We let $\widehat{p}_n^A(x,r|x_0,r_0) = \sum \widehat{p}_n^m$ be the total acoustic contribution at each azimuthal number, which is calculated by summing over all upstream or downstream modes.

We will calculate the derivative of the Wrońskian numerically, by calculating

$$\frac{\partial\mathcal{V}}{\partial\kappa} \approx \frac{\mathcal{V}(\kappa+\varepsilon) - \mathcal{V}(\kappa)}{\varepsilon} \tag{52}$$

for sufficiently small ε such that the derivative has converged. The derivative of the Wrońskian with respect to κ can instead be calculated analytically, although the exact form would be quite complicated. We can calculate the derivative of all the terms in the Wrońskian analytically except the derivatives of ψ_n and Ψ_n, with the latter numerically calculated as

$$\frac{\partial\Psi_n}{\partial\kappa}(r,\kappa_n^m) = \lim_{\varepsilon\to 0} \frac{1}{2}\int_{r_c+\varepsilon}^{r} \frac{\partial q_n}{\partial\kappa}(s,\kappa_n^m)\frac{1}{\sqrt{q_n(s,\kappa_n^m)}}\mathrm{d}s. \tag{53}$$

3.6. Contribution from the critical layer and hydrodynamic modes

We calculate the contribution from the critical layer by using a counter clockwise contour Γ_{CLH} enclosing the critical layer and hydrodynamic modes, which is shown in Figure 3b. We find

$$\widehat{p}_\omega^{\mathrm{CL}}(\boldsymbol{x}|\boldsymbol{x}_0) = \sum_{n=-\infty}^{\infty} \mathrm{e}^{\mathrm{i}n(\theta-\theta_0)}\widehat{p}_n^{\mathrm{CL}}(x,r|x_0,r_0) \text{ where } \widehat{p}_n^{\mathrm{CL}}(x,r|x_0,r_0) = \frac{1}{4\pi^2}\int_{\Gamma_{\mathrm{CLH}}} \widehat{p}_n(r|r_0;\omega,k)\mathrm{e}^{\mathrm{i}k(x-x_0)}\mathrm{d}k. \tag{54}$$

The contribution from the integral around the critical layer is very expensive to calculate numerically, and a method is detailed in Posson and Peake [23, 25]. It is very hard to calculate the critical layer contribution accurately asymptotically, since the high-frequency limit fails to capture most of the behaviour of the critical layer, such as the hydrodynamic modes. An asymptotic method using the high-frequency limit is described in Mathews [17] which produced results of the right order of magnitude but compared poorly to the numerical results. However, it has been suggested that the contribution from the critical layer can generally be ignored [23, 25]. In Posson and Peake [23, Figures 4 and 5] the pressure field due to rotor self-interaction was calculated using a numerical Green's function. For the azimuthal numbers in the figures it was shown that we can ignore the critical layer contribution $\widehat{p}_n^{\mathrm{CL}}$ totally and only use the acoustic Green's function $\widehat{p}_n^A$.

There are some cases where we will have to calculate the critical layer contribution, for example when we have no cut-on eigenmodes. Additionally, when we get unstable hydrodynamic modes, with the condition given in Heaton and Peake [12], we expect the contribution from the critical layer integral to be larger, but in general still considerably smaller than the contribution from the acoustic modes, providing we are not too far downstream of the source, as shown in Posson and Peake [23, Figure 6].

4. Results

We now compare the asymptotic eigenmodes and Green's function to the numerical results, which are calculated using the method set out in Appendix A and Appendix B. We will consider several different swirling flows. The first example is simple polynomial swirl with constant axial flow, while the second example is a more complicated swirling flow involving cases when $q_n(r, \kappa)$ has two zeros. The third example involves a modest frequency, and we show our eigenmodes and Green's function are still reasonably accurate, while the fourth and fifth examples involve industrially realistic swirling flow.

We give all eigenmodes to three decimal places, and label the cut-off eigenmodes outwards from the real axis. We mark any eigenmodes where we need to use the two turning point method with a star in the tables. We calculate the Green's function contribution $\widehat{p}_n^m(x, r | x_0, r_0)$ for each cut-on acoustic mode and the nearest cut-off modes by using Eq. (51). We then sum these contributions to get the acoustic Green's function, $\widehat{p}_n^A$. We generally need to consider the Green's function contribution from at most the closest one or two cut-off modes. This is because the magnitude of the Green's function contribution for the cut-off modes far away from the real line is very small due to the $\exp(\mathrm{i}k(x - x_0))$ term. We only consider the critical layer contribution for the first swirling flow, and we show it is small compared to the acoustic Green's function. We then ignore the critical layer contribution for all other examples, as justified by Posson and Peake [23]. For each example we consider a single source (x_0, r_0) and vary x and r. We always take $x - x_0 > 0$, so we only consider the downstream eigenmodes, but upstream results follow in exactly the same way.

4.1. Simple test case

We consider a simple test case with $U_x = 0.5$, $U_\theta(r) = 0.1r + 0.1/r$, $\omega = 25$, $n = 15$ and both hard and lined walls of impedance $Z_j = 1 - 2\mathrm{i}$. We plot the eigenmodes in Figure 4 and we consider the accuracy of the asymptotic eigenmodes in Table 1. In Figure 4 (and later figures) we distinguish between the asymptotic eigenmodes that are in the region $\mathscr{K}^C$ (green squares) and those in the region $\mathscr{K}$ (yellow circles). In Figures 5 and 6 we plot the Green's function.

4.1.1. Eigenmodes in hard-walled duct

In Figure 4a we see that we are able to find each and every asymptotic eigenmode very accurately. We find there are four cut-on modes with imaginary part zero, and the rest of the modes are cut-off. In the case $U_\theta = 0$ (Example 1 in Mathews [17]) we had six cut-on modes, so the addition of swirl has seen us lose one upstream and one downstream cut-on mode. This is as expected, since the positive azimuthal number corresponds to a co-rotating mode and hence the non-zero, positive swirl has the effect of reducing the phase speed. The four cut-on modes all correspond to a turning point at $r_c \in [h, 1]$ and are very well approximated asymptotically, with the largest relative error 0.0187% in Table 1.

The cut-off modes are also very well approximated. The first two cut-off asymptotic modes lie in $\omega \mathscr{K}$, and are approximated very accurately, with relative errors of 0.0016% and 0.0038% in Table 1. The next two cut-off modes lie outside the region $\omega \mathscr{K}$, and the relative error for these modes is larger, with a relative error of 0.1979% for the third cut-off mode. However, as we consider cut-off modes further from the real line, then the accuracy of the asymptotic modes improves again.

4.1.2. Eigenmodes in lined duct

In Figure 4b and Table 1 we see that the effect of lining shifts the cut-on modes off the real axis and they now have a small imaginary part, which is positive for downstream modes and negative for upstream modes. We again find each eigenmode asymptotically, and the asymptotic modes are again very accurate.
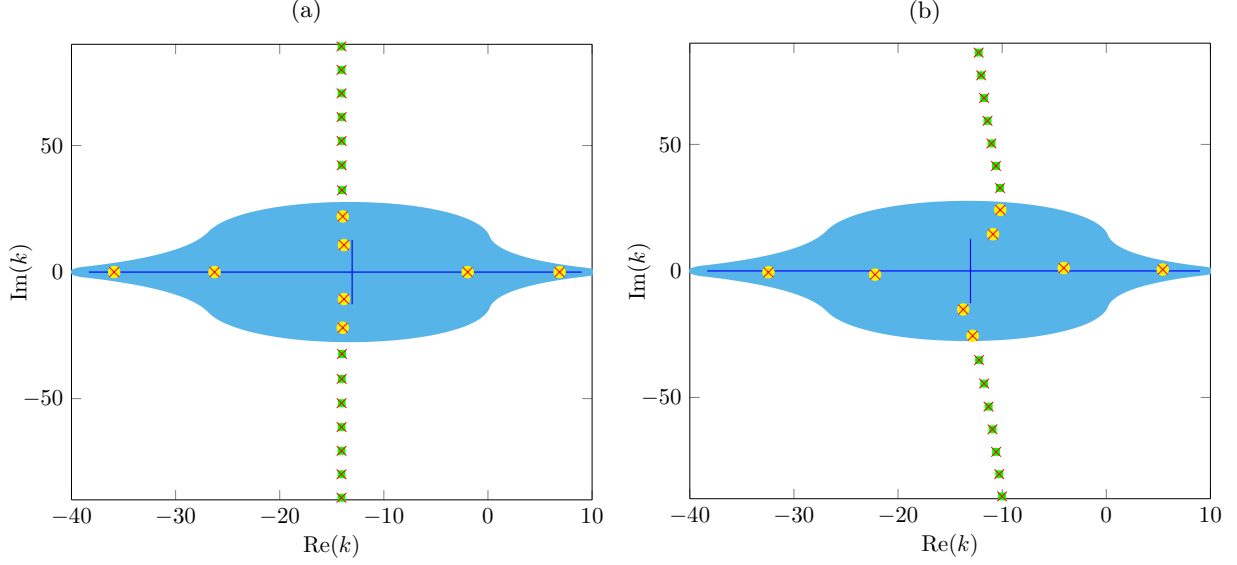
Figure 4: Plot of the asymptotic (green squares/yellow circles) and numerical eigenmodes (red crosses). The parameters are $\omega = 25$, $\eta = 0.6$, $U_x = 0.5$, $U_\theta(r) = 0.1r + 0.1/r$, $h = 0.6$ with (a) hard walls; (b) lined walls of impedance $Z_j = 1 - 2i$. In blue is the region $\omega\mathcal{K}$.

Table 1: Asymptotic eigenmodes in a hard-walled duct from Figure 4a and lined duct from Figure 4b. We have only considered the first four cut-off modes. The error is the relative error, given by calculating $|k_{\mathrm{asy}} - k_{\mathrm{num}}|/|k_{\mathrm{num}}|$.

		Hard walled			Lined walls with $Z_j = 1 - 2i$		
		Asymptotic	Numerical	Error	Asymptotic	Numerical	Error
Cut-on		-35.898	-35.898	0.0015%	$-32.450 - 0.523i$	$-32.449 - 0.523i$	0.0019%
		-26.263	-26.262	0.0019%	$-22.209 - 1.452i$	$-22.208 - 1.452i$	0.0039%
		-1.948	-1.949	0.0187%	$-4.090 + 1.127i$	$-4.091 + 1.128i$	0.0219%
		6.877	6.876	0.0110%	$5.419 + 0.553i$	$5.418 + 0.553i$	0.0172%
Cut-off		$-13.835 \pm 10.670i$	$-13.835 \pm 10.670i$	0.0016%	$-12.843 - 25.629i$	$-12.844 - 25.629i$	0.0045%
		$-13.951 \pm 21.985i$	$-13.952 \pm 21.985i$	0.0038%	$-13.738 - 15.230i$	$-13.738 - 15.230i$	0.0037%
		$-14.003 \pm 32.386i$	$-14.022 + 32.319i$	0.1979%	$-10.880 + 14.498i$	$-10.880 + 14.499i$	0.0051%
		$-14.037 \pm 42.217i$	$-14.046 \pm 42.189i$	0.0658%	$-10.182 + 24.094i$	$-10.183 + 24.095i$	0.0045%

In the table we find that the asymptotic cut-on modes are slightly less accurate than when we had no lining, although the largest relative error is only 0.0219%. The cut-off modes are similarly accurate again, with a jump in the relative error as we move out of the $\omega\mathcal{K}$ region.

We could also give the error in the rate of decay (in dB per radius), which we calculate as

$$20 \log_{10} \exp(\mathrm{Im}(k_{\mathrm{asy}} - k_{\mathrm{num}})). \tag{55}$$

However, for Table 1 we find this error is less than 1×10^{-2}dB for all the eigenmodes.

4.1.3. Green's function in a hard-walled duct

We consider a single source at $r_0 = 0.8$ and $x - x_0 = 0.5$, so we only need to consider the contribution from the downstream eigenmodes. There are two downstream cut-on modes and we see their Green's function contributions $\widehat{p}_n^m$ in Figures 5a and 5b. We see the asymptotic Green's function very accurately approximates the numerical Green's function for these cut-on modes.

The Green's function associated with the first cut-off mode in Figure 5c is several orders of magnitude smaller than the cut-on modes, but still approximates the numerical Green's function extremely well. In Figure 5d we plot the Green's function contribution from the second cut-off mode and see that the asymptotic Green's function is again very accurate, but is even smaller in magnitude than the contribution from the first cut-off mode. In Figure 5e we see the contribution of the critical layer $\widehat{p}_n^{\mathrm{CL}}$ numerically. As expected,
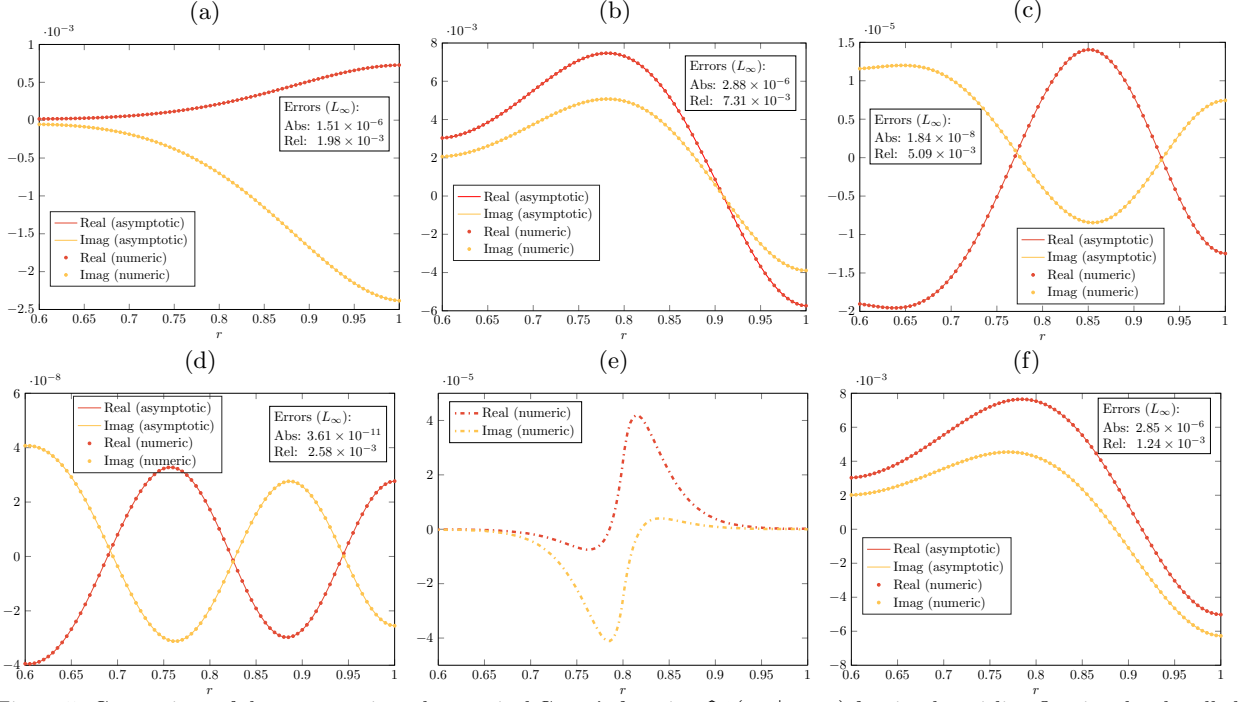
13

Figure 5: Comparison of the asymptotic and numerical Green's function $\widehat{p}_n^m(x, r|x_0, r_0)$ for simple swirling flow in a hard-walled duct. Contribution from (a) $k = 6.877$; (b) $k = -1.948$; (c) $k = -13.835 + 10.670i$; (d) $k = -13.951 + 21.985i$. (e) Critical layer contribution $\widehat{p}_n^{\mathrm{CL}}(x, r|x_0, r_0)$; (f) Total acoustic Green's function $\widehat{p}_n^A(x, r|x_0, r_0)$. The source is at $r_0 = 0.8$ and $x - x_0 = 0.5$, and the other parameters are given in Figure 4.

the critical layer contribution is several orders of magnitude smaller than the contribution from the cut-on modes, and of a similar magnitude to the contribution from the first cut-off mode. In each figure we give the relative and absolute error of the asymptotic result compared to the numerical result, using the L_∞ norm.

Finally, in Figure 5f we see the sum of the contributions from Figures 5a to 5d, giving the acoustic Green's function $\widehat{p}_n^A$. The acoustic Green's function can be attributed almost entirely to the single eigenmode $k = -1.948$. The absolute error in the asymptotic Green's function compared to the numerical results is $\mathcal{O}(10^{-6})$, with a relative error of $\mathcal{O}(10^{-3})$. Since we threw away $\mathcal{O}(\omega^{-2})$ terms in our differential equation in Eq. (25), the relative error is about what we expect, and shows the usefulness of the asymptotics for typical engine parameters. However, although the relative error is $\mathcal{O}(\omega^{-2})$, we will see later that the error very much depends on the form of the swirling flow, with more complicated flows having a significant greater (around ten times) relative error.

4.1.4. Green's function in a lined duct

In Figure 6 we see the Green's function for the same simple swirling flow, but in a lined duct. In Figures 6a and 6b we see the asymptotic Green's function contributions $\widehat{p}_n^m$ from the cut-on modes very accurately approximate the numerical Green's function. Furthermore, the cut-on mode $k = -4.090 + 1.128i$ dominates the total acoustic Green's function $\widehat{p}_n^A$ in Figure 6f. This mode is the counterpart of the dominant mode $k = -1.948$ in a hard-walled duct.

In Figures 6c and 6d we plot the Green's function contribution $\widehat{p}_n^m$ from the first and second cut-off modes, which are $\mathcal{O}(10^{-6})$ and $\mathcal{O}(10^{-8})$ respectively, so three and five orders of magnitude smaller than the dominant cut-on modes. The asymptotic Green's function from these modes is still extremely accurate compared to the numerical Green's function. In Figure 6e we see the asymptotic Green's function contribution from the third cut-off mode, which is $\mathcal{O}(10^{-10})$, so seven orders of magnitude smaller than the dominant cut-on modes. However, the Green's function is slightly less accurate for this mode, because it only just lies outside the region $\mathscr{K}$ but we use the zero turning point solution. The contribution from the critical layer is very similar to that in Figure 5e, with the lining shown to have next to no effect on the critical layer contribution
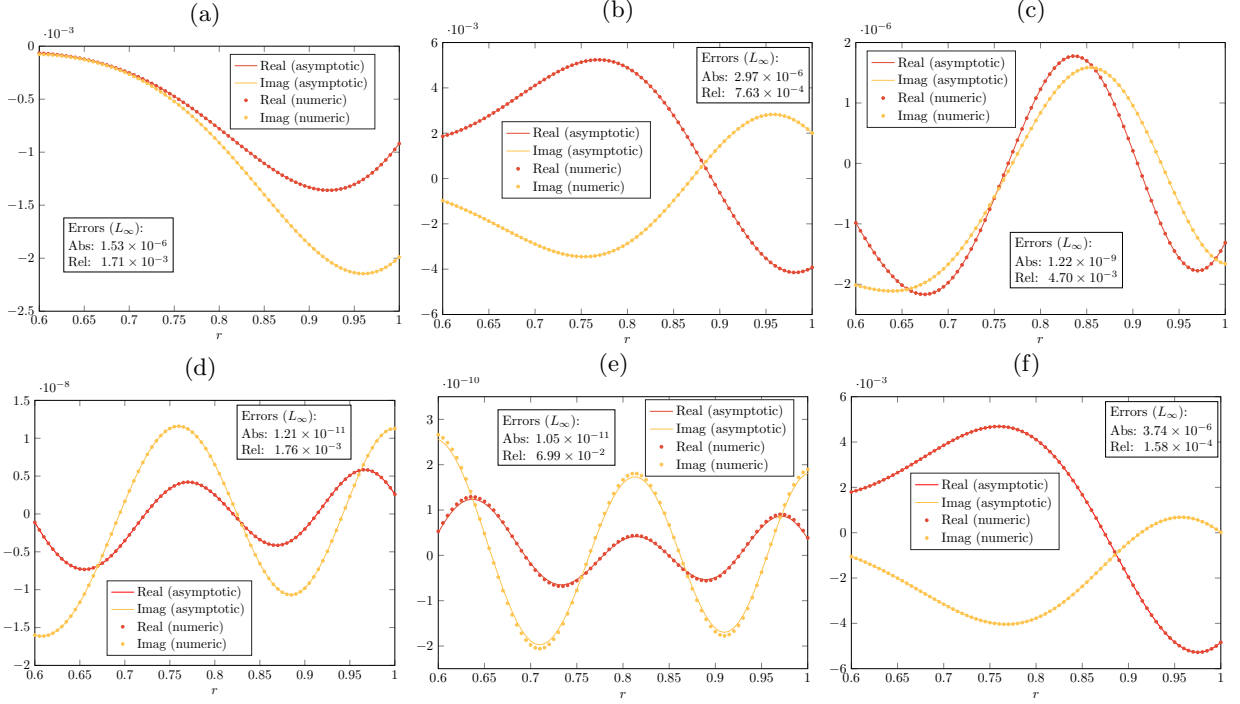
14

Figure 6: Comparison of the asymptotic and numerical Green's function $\widehat{p}_n^m(x, r|x_0, r_0)$ for simple swirling flow in a lined duct of impedance $Z_j = 1 - 2i$. Contribution from (a) $k = 5.419 + 0.553i$; (b) $k = -4.090 + 1.128i$; (c) $k = -10.880 + 14.498i$; (d) $k = -10.182 + 24.094i$; (e) $k = -10.202 + 32.819i$. (f) Total acoustic Green's function $\widehat{p}_n^A(x, r|x_0, r_0)$. The source is at $r_0 = 0.8$ and $x - x_0 = 0.5$, and the other parameters are given in Figure 4.

and hydrodynamic modes in Posson and Peake [24]. In Figure 6f we plot the acoustic Green's function $\widehat{p}_n^A$, and we find the absolute error in the asymptotic Green's function compared to the numerical results is again $\mathcal{O}(10^{-6})$.

4.1.5. Effect of swirl on the Green's function

So far, all of our results have considered just a single azimuthal mode. If we want to calculate the Green's function G_ω or $\widehat{p}_\omega$ then we have to sum over all azimuthal modes. For large values of n, we find that there
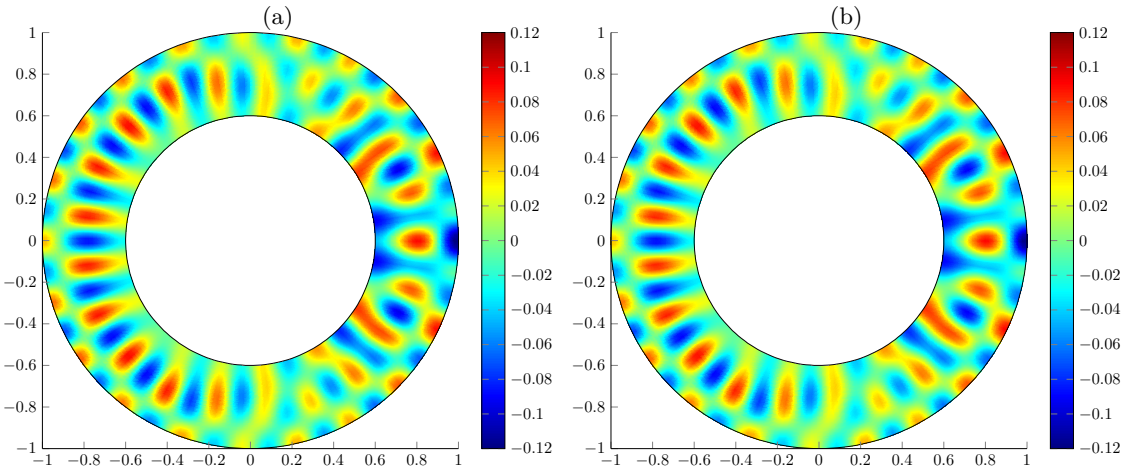

Figure 7: Colour plot of the Green's function for no swirl ($U_\theta = 0$). (a) Real part of numerical acoustic Green's function $\widehat{p}_\omega^A(\boldsymbol{x}|\boldsymbol{x}_0)$; (b) real part of asymptotic acoustic Green's function $\widehat{p}_\omega^A(\boldsymbol{x}|\boldsymbol{x}_0)$. The source is given by $(r_0, \theta_0) = (0.8, 0)$ and $x - x_0 = 0.5$. The other flow parameters are $U_x = 0.5$, hard walls, $\omega = 25$ and $h = 0.6$.
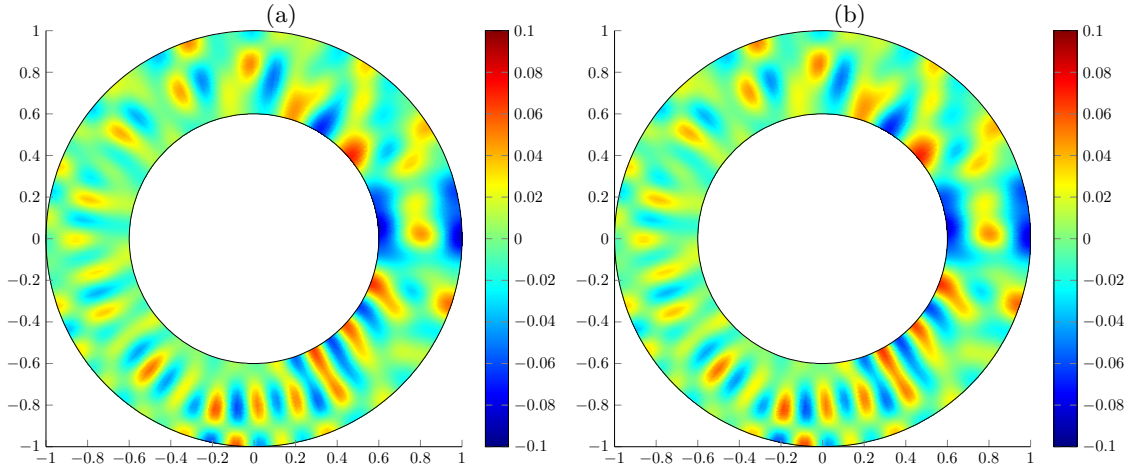
15

Figure 8: Colour plot of the Green's function for swirl $U_\theta(r) = 0.1r + 0.1/r$. (a) Real part of numerical acoustic Green's function $\widehat{p}_\omega^A(\boldsymbol{x}|\boldsymbol{x}_0)$; (b) real part of asymptotic acoustic Green's function $\widehat{p}_\omega^A(\boldsymbol{x}|\boldsymbol{x}_0)$. The other parameters are as in Figure 7.

are no cut-on eigenmodes and thus the contribution to the total Green's function is very small. We find the dominant behaviour of the total Green's function is determined by azimuthal numbers $n = \mathcal{O}(\omega)$, like in Wundrow and Khavaran [35].

In Figures 7 and 8 we plot the real parts of the asymptotic and numerical acoustic Green's function $\widehat{p}_\omega^A$ as a function of r and θ for a fixed value of x. We consider a single source with $r_0 = 0.8$, $\theta_0 = 0$ and $x - x_0 = 0.5$ in a hard-walled duct. We consider the same uniform axial flow as before, and compare the Green's function with zero swirl (Figures 7a and 7b) to when the swirl is non-zero and given by $U_\theta(r) = 0.1r + 0.1/r$ (Figures 8a and 8b). We see excellent agreement between the numerical and asymptotic Green's function regardless of the swirling component of the flow.

The effect of swirl is very clear in the figure, with significantly different colour maps. The swirl causes the Green's function to be significantly less uniform circumferentially. When we have no swirl, the Green's function has two distinct regions. For $-\pi/2 \lesssim \theta \lesssim \pi/2$ the Green's function has a complicated azimuthal structure, being the superposition of several modes. For $\pi/2 \lesssim \theta \lesssim \pi$ and $-\pi \lesssim \theta \lesssim \pi/2$ the Green's function has rotational symmetry, and is apparently dominated by an azimuthal mode of order $n = 20$. The Green's function is also symmetric along the horizontal axis. When we introduce swirl, the Green's function no longer has any symmetry.

4.2. More complicated flow with two turning points

We now consider a more complicated swirling flow, with $U_x(r) = 0.2 + 0.4r^2 - 0.3r^3$ and $U_\theta(r) = 0.1r + 0.2/r + 0.3r^2$, in a lined duct of impedance $Z_j = 1 - 2i$. We consider $\omega = 25$ and the counter-rotating mode $n = -20$, which gives us both upstream and downstream cut-on asymptotic modes where $q_n(r, \kappa)$ has two zeros. The eigenmodes are plotted in Figure 9, and the region where $q_n(r, \kappa)$ has two or more zeros is shaded in black. In this region we need to use the method in Section 3.3 to calculate the eigenmodes. It takes longer to calculate eigenmodes in the shaded region than other eigenmodes, due to having to find the null space of a differential equation rather than being able to write down the solution.

We find four cut-on asymptotic modes in the region where $q_n(r, \kappa)$ has two or more zeros, which are the two furthest upstream modes, and the second and third furthest downstream modes, marked with a star in the table in Figure 9 and plotted in orange diamonds in the figure. The accuracy of these modes is very similar to the accuracy of the other eigenmodes, which were obtained using the method in Section 3.2. However, because of the higher order polynomials in the swirling flow, the accuracy of all the eigenmodes is worse than in Section 4.1, by a factor of around 10, although still very favourable. We could again calculate the error in the rate of decay, using Eq. (55), although we again find it is less than 6×10^{-2}dB per radius.

We next plot the Green's function contribution from each of the five downstream cut-on eigenmodes, and the total Green's function in Figure 10. The contribution from the cut-on modes are all $\mathcal{O}(10^{-3})$, while
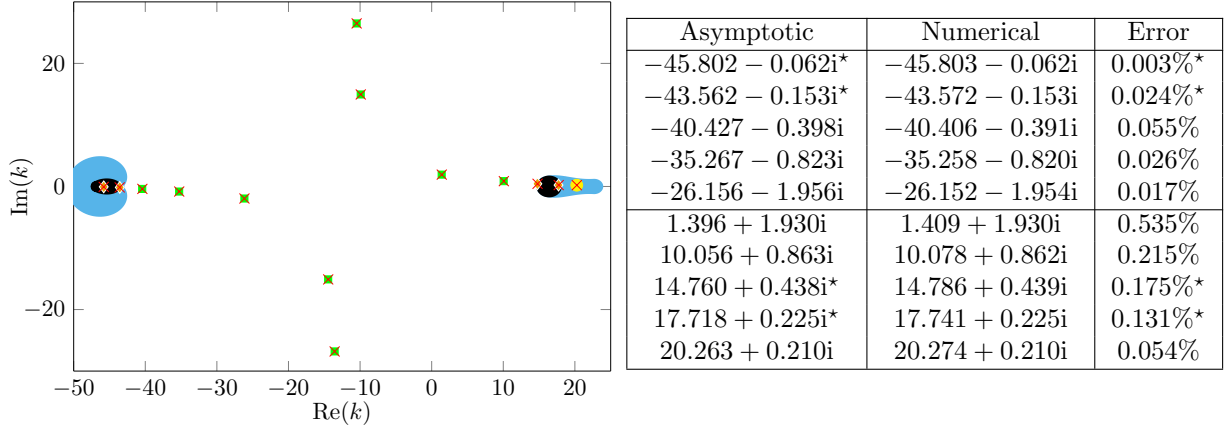
16

Asymptotic	Numerical	Error
$-45.802 - 0.062i^\star$	$-45.803 - 0.062i$	$0.003\%^\star$
$-43.562 - 0.153i^\star$	$-43.572 - 0.153i$	$0.024\%^\star$
$-40.427 - 0.398i$	$-40.406 - 0.391i$	0.055%
$-35.267 - 0.823i$	$-35.258 - 0.820i$	0.026%
$-26.156 - 1.956i$	$-26.152 - 1.954i$	0.017%
$1.396 + 1.930i$	$1.409 + 1.930i$	0.535%
$10.056 + 0.863i$	$10.078 + 0.862i$	0.215%
$14.760 + 0.438i^\star$	$14.786 + 0.439i$	$0.175\%^\star$
$17.718 + 0.225i^\star$	$17.741 + 0.225i$	$0.131\%^\star$
$20.263 + 0.210i$	$20.274 + 0.210i$	0.054%

Figure 9: Plot of the asymptotic (green squares/yellow circles/orange diamonds) and numerical eigenmodes (red crosses) and corresponding table. The error in the eigenmodes is calculated as $|k_{\mathrm{asy}} - k_{\mathrm{num}}|/|k_{\mathrm{num}}|$. The parameters are $\omega = 25$, $n = -20$, $h = 0.5$, $U_x = 0.2 + 0.4r^2 - 0.3r^3$, $U_\theta(r) = 0.1r + 0.2/r + 0.3r^2$ with lined walls of impedance $Z_j = 1 - 2i$. In blue is the region $\omega\mathcal{K}$ and in black is where $q_n(r, \kappa)$ has two or more zeros.
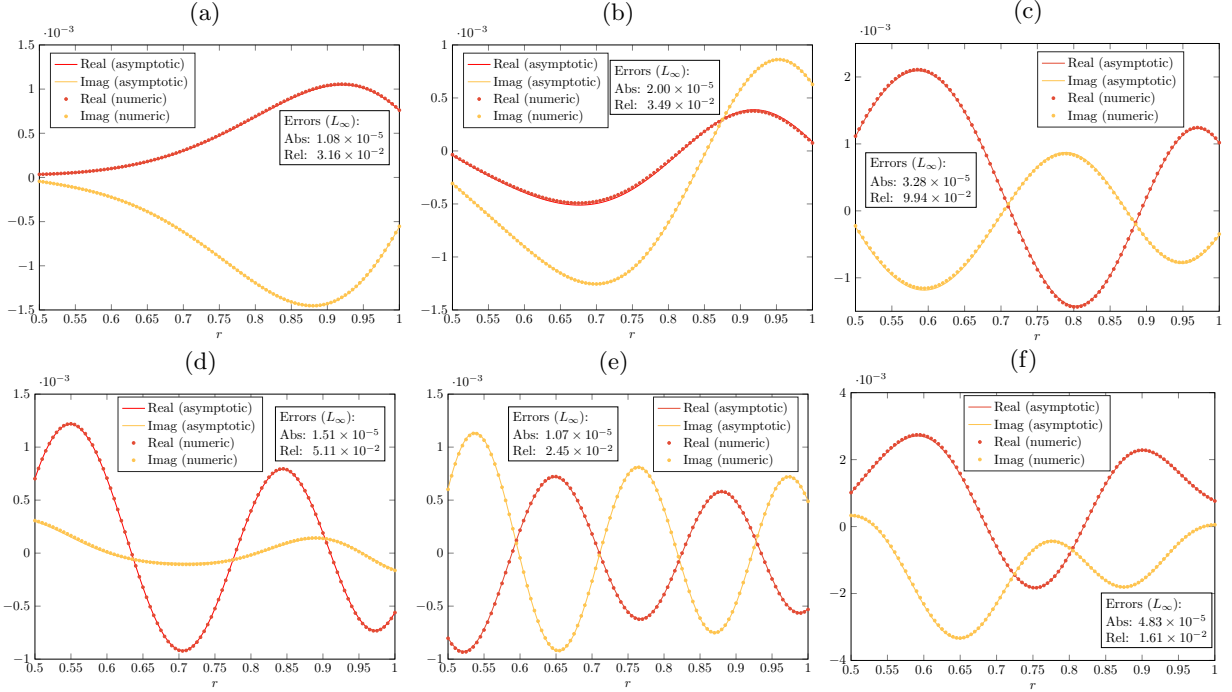

Figure 10: Comparison of the asymptotic and numerical Green's function $\widehat{p}_n^m(x, r | x_0, r_0)$ for complicated swirling flow in a lined duct of impedance $Z_j = 1 - 2i$. Contribution from (a) $k = 20.263 + 0.210i$; (b) $k = 17.718 + 0.225i^\star$; (c) $k = 14.760 + 0.438i^\star$; (d) $k = 10.056 + 0.863i$; (e) $k = 1.396 + 1.930i$. (f) Total acoustic Green's function $\widehat{p}_n^A(x, r | x_0, r_0)$. The source is at $r_0 = 0.8$ and $x - x_0 = 0.5$, and the other parameters are given in Figure 9.

the contribution from the first cut-off mode is $\mathcal{O}(10^{-6})$.

In Figure 10 we see that the asymptotic Green's function is extremely accurate for each of the downstream cut-on modes, as is the total Green's function. For the eigenmodes in Figures 10b and 10c we have two zeros of $q_n(r, \kappa)$, and we find the asymptotic Green's function is slightly less accurate, with the absolute error of the asymptotic Green's function compared to the numerical Green's function $\mathcal{O}(10^{-5})$. For the other eigenmodes, we have a single zero or no zeros of $q_n(r, \kappa)$ but the absolute error of the asymptotic Green's function compared to numerical results is still $\mathcal{O}(10^{-5})$. The absolute error of the total asymptotic Green's function is $\mathcal{O}(10^{-5})$, while the relative error is $\mathcal{O}(10^{-2})$.

17

4.3. Swirling flow at moderate frequency

Next, we investigate how our high-frequency asymptotics perform at moderate frequencies. We use the swirling flow from Section 4.2 in a lined duct of impedance $Z_j = 1 - 2i$, but now we set $\omega = 12$ and $n = 5$. In Figure 11 we see a plot and a table of the asymptotic and numerical eigenmodes. We can see in Figure
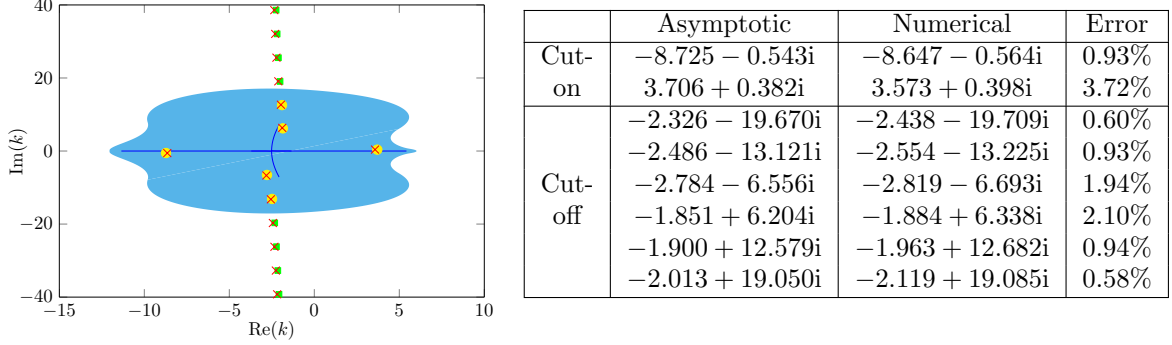

		Asymptotic	Numerical	Error
Cut-		$-8.725 - 0.543i$	$-8.647 - 0.564i$	0.93%
on		$3.706 + 0.382i$	$3.573 + 0.398i$	3.72%
		$-2.326 - 19.670i$	$-2.438 - 19.709i$	0.60%
		$-2.486 - 13.121i$	$-2.554 - 13.225i$	0.93%
Cut-		$-2.784 - 6.556i$	$-2.819 - 6.693i$	1.94%
off		$-1.851 + 6.204i$	$-1.884 + 6.338i$	2.10%
		$-1.900 + 12.579i$	$-1.963 + 12.682i$	0.94%
		$-2.013 + 19.050i$	$-2.119 + 19.085i$	0.58%

Figure 11: Plot of the asymptotic (green squares/yellow circles) and numerical eigenmodes (red crosses) and corresponding table. The error in the eigenmodes is calculated as $|k_{\text{asy}} - k_{\text{num}}|/|k_{\text{num}}|$. The parameters are $\omega = 12$, $n = 5$, $U_x = 0.2 + 0.4r^2 - 0.3r^3$, $U_\theta(r) = 0.1r + 0.2/r + 0.3r^2$, $h = 0.5$ with lined walls of impedance $Z_j = 1 - 2i$. In blue is the region $\omega \mathcal{K}$.

11 that we approximate the eigenmodes reasonably well, although the accuracy is considerably worse that when we had the same swirling flow at $\omega = 25$ in the previous section.

In Figure 12 we plot the acoustic Green's function, obtained by summing up the contribution from each eigenmode. We consider the upstream Green's function when $x - x_0 = -0.5$ in Figure 12 and the downstream Green's function when $x - x_0 = 0.5$ in Figure 12. We see reasonable agreement between the
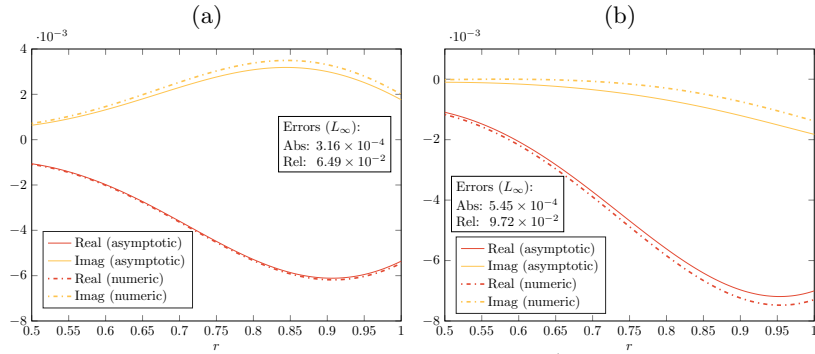

Figure 12: Comparison of the asymptotic and numerical Green's function $\hat{p}_n^A(x, r | x_0, r_0)$ for the swirling flow in Figure 11 in a lined duct of impedance $Z_j = 1 - 2i$. The source is at $r_0 = 0.8$ and (a) $x - x_0 = -0.5$; (b) $x - x_0 = 0.5$.

asymptotic and numerical Green's function, with the error between the Green's function sufficiently small that the asymptotic results could be used in practice as a good substitute. The non-dimensional frequency of $\omega = 12$ corresponds to a frequency of around 450Hz on a modern aeroengine, which shows our asymptotic Green's function would be suitable in most realistic frequency ranges. If we made the frequency smaller still then our results become more and more inaccurate, and in this case seem of little practical use for $\omega < 10$.

4.4. Realistic swirling flow at low speed

We next consider realistic swirling flow at low speed, with the mean flow profiles given in Figure 13. These realistic flow profiles are based on CFD calculations, and we have considered the swirling flow between the rotor and the stator, ignoring the boundary layers of the mean flow. The other parameters we consider are $h = 0.4$, $n = 7$ and $\omega = 22$ (which is close to the first blade passing frequency). We consider both hard walls and lined walls of impedance $Z_j = 1 - 2i$. In Figure 14 we plot the eigenmodes and in Table 2 we compare the accuracy of the asymptotic eigenmodes to the numerical eigenmodes. In Figures 15 and 16 we plot the Green's function.
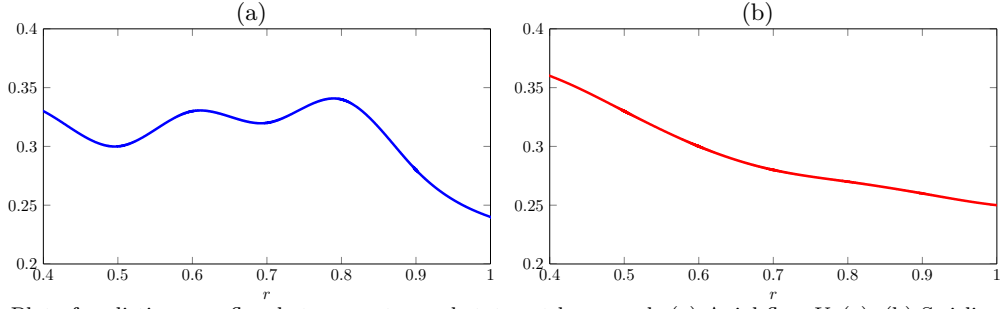
18

Figure 13: Plot of realistic mean flow between rotor and stator at low speed. (a) Axial flow $U_x(r)$; (b) Swirling flow $U_\theta(r)$.
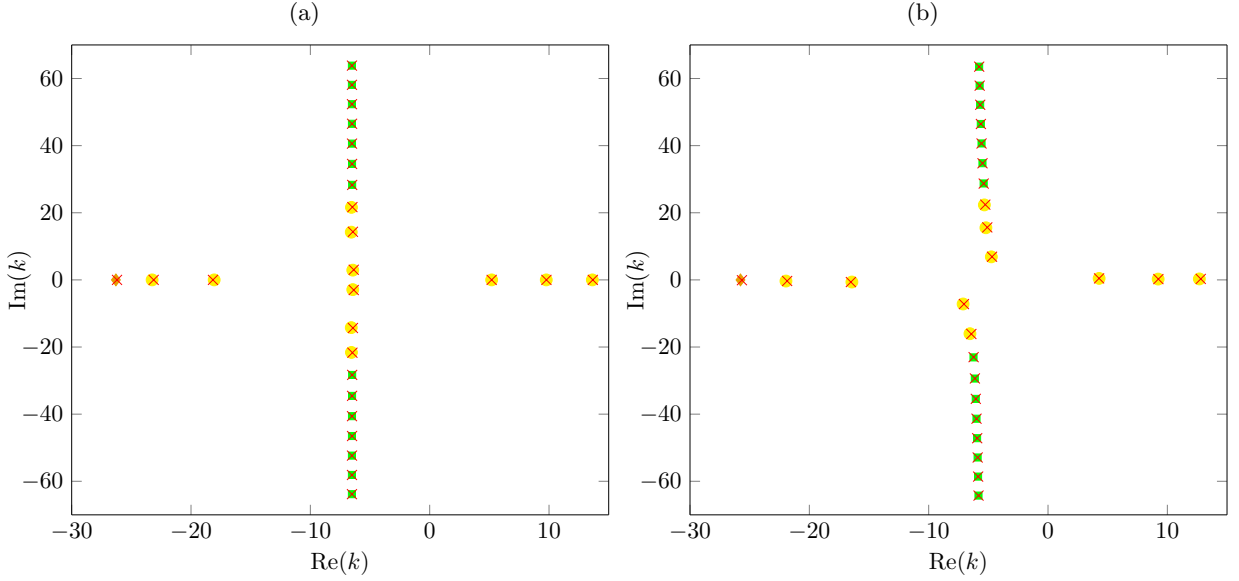

Figure 14: Plot of the asymptotic (green squares/yellow circles/orange diamonds) and numerical eigenmodes (red crosses). The flow is given by Figure 13, with other parameters given by $\omega = 22$, $n = 7$, $h = 0.4$ with (a) hard walls; (b) lined walls of impedance $Z_j = 1 - 2i$.

4.4.1. Eigenmodes in hard-walled duct

We plot the eigenmodes in Figure 14a, and we clearly see that despite the more complicated swirling flow, we asymptotically approximate all the numerical modes accurately in Table 2.

Table 2: Asymptotic and numerical eigenmodes from Figure 14. The error in the eigenmodes is calculated as $|k_{\text{asy}} - k_{\text{num}}|/|k_{\text{num}}|$.

		Hard walled		Lined walls with $Z_j = 1 - 2i$		
	Asymptotic	Numerical	Error	Asymptotic	Numerical	Error
Cut-on	$-26.2931^\star$	-26.248	$0.17\%^\star$	$-25.771 - 0.092i^\star$	$-25.693 - 0.097i$	$0.30\%^\star$
	-23.259	-23.142	0.51%	$-21.962 - 0.347i$	$-21.878 - 0.324i$	0.40%
	-18.056	-18.199	0.47%	$-16.435 - 0.635i$	$-16.556 - 0.642i$	0.74%
	5.193	5.221	0.53%	$4.282 + 0.446i$	$4.310 + 0.446i$	0.64%
	9.769	9.800	0.31%	$9.229 + 0.239i$	$9.264 + 0.241i$	0.37%
	13.628	13.692	0.79%	$12.677 + 0.290i$	$12.824 + 0.288i$	1.15%
Cut-off	$-6.572 - 14.215i$	$-6.437 - 14.292i$	0.48%	$-6.542 - 16.029i$	$-6.429 - 16.096i$	0.76%
	$-6.446 - 2.905i$	$-6.372 - 2.850i$	2.85%	$-7.116 - 7.179i$	$-7.062 - 7.152i$	0.60%
	$-6.446 + 2.905i$	$-6.372 + 2.850i$	2.85%	$-4.751 + 6.867i$	$-4.685 + 6.847i$	0.83%
	$-6.572 + 14.215i$	$-6.437 + 14.292i$	0.48%	$-5.204 + 15.525i$	$-5.089 + 15.616i$	0.89%

19

The most cut-on upstream mode lies in a region where $q_n(r, \kappa)$ has two or more zeros, and hence we have to use Section 3.3 to find it asymptotically, and we plot it in orange in Figure 14a. The accuracy of the eigenmodes is slightly worse than when we had polynomial swirling flow, although the asymptotic modes are still quite accurate. The error is larger because of the more complicated swirling flow profiles, since we now have to use high order polynomials (with order greater than ten) to approximate the mean flows.

4.4.2. Eigenmodes in a lined duct

In Figure 14b, we see the effect of realistic swirling flow on the eigenmodes in a lined duct. We see that they are quite accurate compared to the numerical modes in Table 2, although again the accuracy is slightly worse than when we had polynomial swirling flow. The accuracy is comparable to when we have hard walls, so the introduction of lining has not changed the accuracy.

The introduction of lining breaks the symmetry of the cut-off modes about the real line and shifts most of them to the right, and further from the real line. If we instead consider negative values of the azimuthal number, then we find the cut-off modes still shift right when we introduce lining, but they move closer to the real line. Thus, counter-rotating modes are less effectively damped by the lining, in agreement with Cooper and Peake [4]. The lining also shifts the cut-on modes off the real line. It is interesting to note that the furthest downstream cut-on mode has a larger imaginary part than the next downstream cut-on mode, which is something not to be expected based on the previous examples.

We could again calculate the error in the rate of decay, using Eq. (55). We now find the error is significantly larger that the previous examples, with the largest error for the cut-on modes being around 0.2dB per radius.

4.4.3. Green's function in hard-walled duct

In Figure 15 we consider the Green's function for the realistic swirling flow given in Figure 13 in hard-walled duct. We consider the contributions $\widehat{p}_n^m$ from the three cut-on modes and the first two cut-off modes.
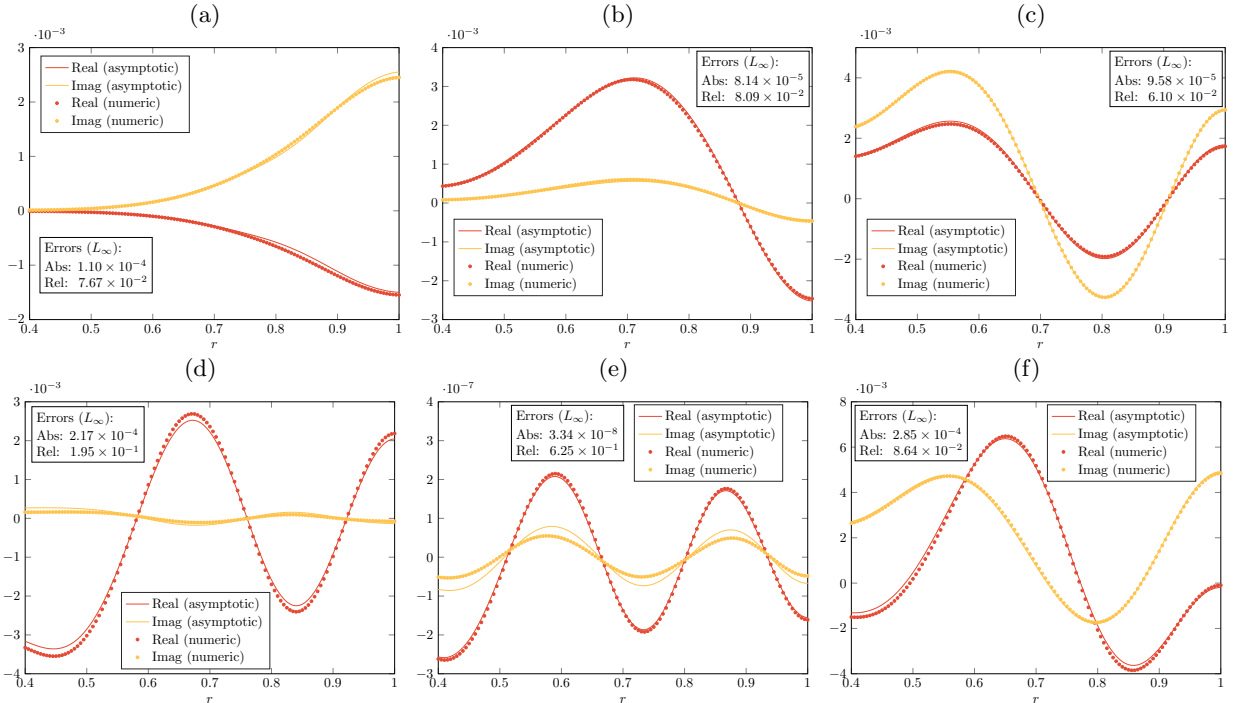

Figure 15: Comparison of the asymptotic and numerical Green's function $\widehat{p}_n^m(x, r | x_0, r_0)$ for realistic low speed mean flow in a hard-walled duct. Contribution from (a) $k = 13.628$; (b) $k = 9.769$; (c) $k = 5.193$; (d) $k = -6.445 + 2.905i$ (e) $k = -6.572 + 14.215i$. (f) Total acoustic Green's function $\widehat{p}_n^A(x, r | x_0, r_0)$. The source is at $r_0 = 0.8$ and $x - x_0 = 0.5$, and the other parameters are given in Figure 14.

The first of these cut-off modes, at $k = -6.445 + 2.905$i, only has a small imaginary part and the Green's function contribution from this mode, in Figure 15d, is of a similar magnitude, $\mathcal{O}(10^{-3})$, to the Green's function contribution from the cut-on modes in Figures 15a, 15b and 15c. Unlike when we had simple swirling flow in Section 4.1, there is no single dominant eigenmode. The contribution to the Green's function from the second cut-off mode, at $k = -6.572 + 14.215$i, is $\mathcal{O}(10^{-7})$ so it is insignificant compared to the other modes.

The accuracy of the asymptotic Green's function for each mode is very good and compares extremely favourably to the numerical results. For the first and second cut-off modes, in Figures 15d and 15e, the amplitude of the asymptotic Green's function is not perfect, but otherwise the asymptotic results are very good. The error in the asymptotic Green's function in these two figures is due to the errors in the asymptotic eigenmodes. In Figure 15f we see the total acoustic Green's function $\widehat{p}_n^A$, and the absolute error between the asymptotic and numerical Green's function is $\mathcal{O}(10^{-4})$ and is barely visible in the figure.

4.4.4. Green's function in a lined duct

In Figure 16 we calculate the Green's function contributions $\widehat{p}_n^m$ for the realistic swirling flow in a lined duct. The first thing we see is that asymptotic Green's function is very accurate when we compare it to the numerical Green's function, although not as accurate as when we had simple swirling flow in a lined duct. Only in Figures 16a and 16e is the asymptotic Green's function inaccurate, which is due to discrepancies in the asymptotic eigenmodes.

Unlike when we had hard walls, the contribution from the first cut-off mode in Figure 16d is one order of magnitude smaller than the contributions from the cut-on modes. The contribution from the second cut-off mode in Figure 16e is again $\mathcal{O}(10^{-7})$, and all subsequent cut-off modes have even smaller contributions. Thus, the total acoustic Green's function $\widehat{p}_n^A$ in Figure 16f only depends on the three cut-on modes. The absolute error in the asymptotic acoustic Green's function compared to the numerical Green's function is again $\mathcal{O}(10^{-4})$ (but only just), and most of this error can be attributed to the Green's function contribution
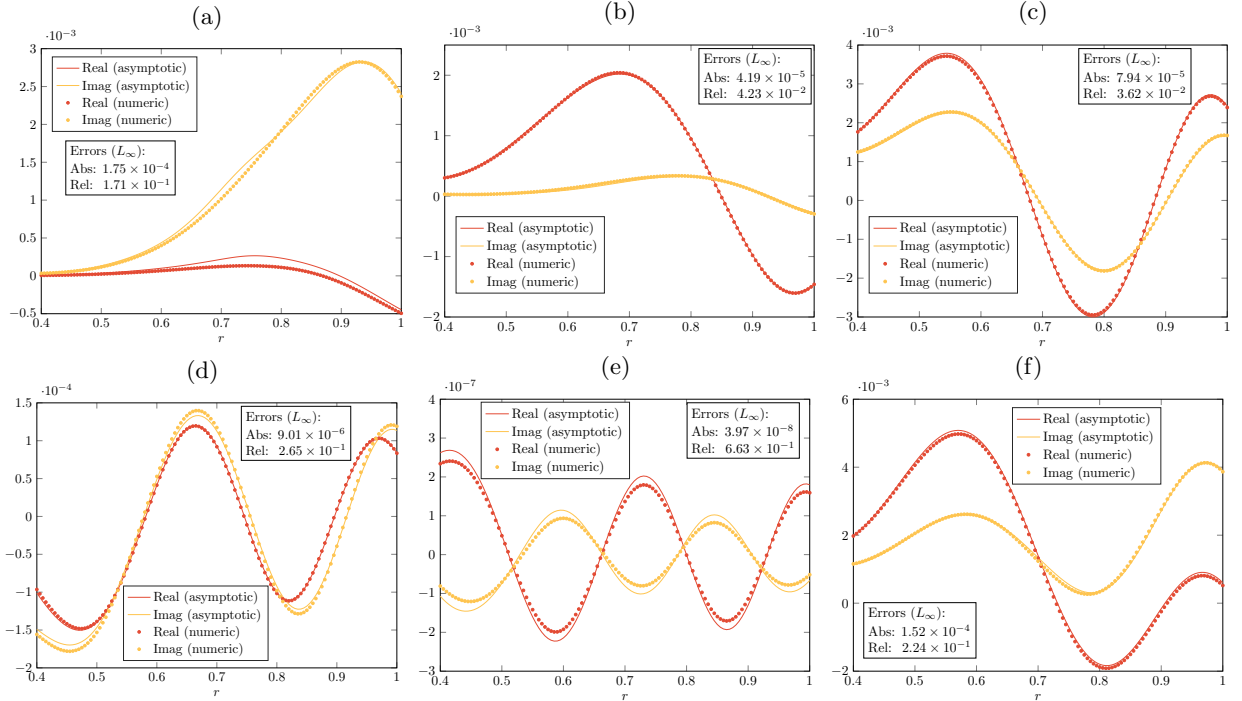

Figure 16: Comparison of the asymptotic and numerical Green's function $\widehat{p}_n^m(x, r | x_0, r_0)$ for realistic low speed mean flow in a lined duct of impedance $Z_j = 1 - 2$i. Contribution from (a) $k = 12.677 + 0.290$i; (b) $k = 9.229 + 0.239$i; (c) $k = 4.282 + 0.446$i; (d) $k = -4.751 + 6.867$i; (e) $k = -5.204 + 15.525$i. (f) Total acoustic Green's function $\widehat{p}_n^A(x, r | x_0, r_0)$. The source is at $r_0 = 0.8$ and $x - x_0 = 0.5$, and the other parameters are given in Figure 14.
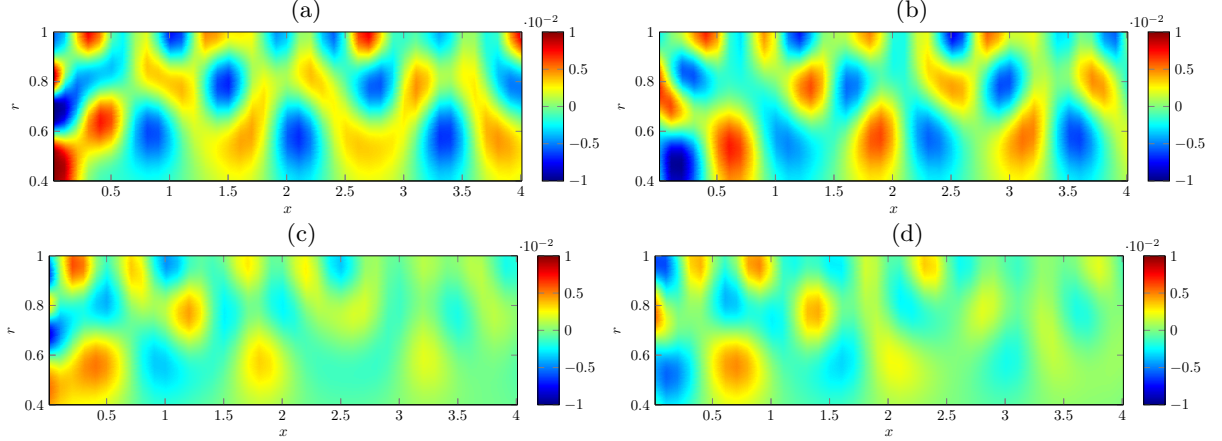
21

Figure 17: Colour plot of the asymptotic acoustic Green's function $\widehat{p}_n^A(x, r | x_0, r_0)$ with a source at $(x_0, r_0) = (0, 0.8)$ as x and r vary. (a) $\mathrm{Re}(\widehat{p}_n^A)$ in hard-walled duct; (b) $\mathrm{Im}(\widehat{p}_n^A)$ in hard-walled duct, (c) $\mathrm{Re}(\widehat{p}_n^A)$ in a lined duct with impedance $Z_j = 1 - 2\mathrm{i}$; (d) $\mathrm{Im}(\widehat{p}_n^A)$ in a lined duct with impedance $Z_j = 1 - 2\mathrm{i}$.

from the asymptotic eigenmode $k = 12.677 + 0.290\mathrm{i}$.

In Figure 17 we plot the real and imaginary part of the asymptotic Green's function $\widehat{p}_n^A$ for the realistic swirling flow. We consider a point source at $(x_0, r_0) = (0, 0.8)$ and vary x and r. The numerical results would be very similar, and we do not plot them here. We expect the absolute error between the asymptotic Green's function and the numerical Green's function as we vary x to be very similar to the error in Figure 16f. We clearly see the effect of the lining in Figures 17c and 17d. The presence of lining changes the magnitude of the Green's function and makes it decay in the axial direction.

4.5. Realistic swirling flow at high speeds

Finally, we consider realistic swirling flow at high speed, with the mean flow profiles given in Figure 18. We again ignore the boundary layers of the flow. We now consider a frequency of $\omega = 19.5$. We only consider a lined duct, with impedance at both duct walls of $Z_j = 1 - 2\mathrm{i}$.
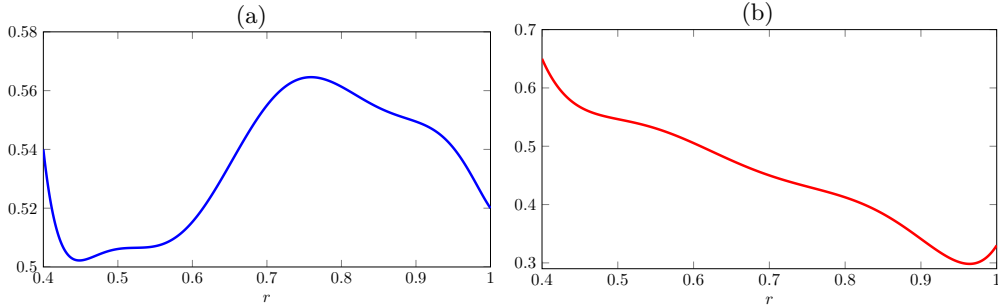

Figure 18: Plot of realistic mean flow between rotor and stator at high speed in a lined duct. (a) Axial flow $U_x(r)$; (b) Swirling flow $U_\theta(r)$.

We compare the asymptotic acoustic Green's function $\widehat{p}_n^A$ to the numerical acoustic Green's function in Figure 19 as we vary both x and r for a single source point at $(x_0, r_0) = (0, 0.8)$. We see that the asymptotic results agree extremely favourably with the numerical results. We get two downstream eigenmodes which are close to cut-on (with $|\mathrm{Im}(k)| < 1$), and the Green's function contribution from both of these eigenmodes is $\mathcal{O}(10^{-3})$. These are the dominant contributions to the Green's function, with the magnitude of the Green's function contribution from the first cut-off mode $\mathcal{O}(10^{-5})$, and the second cut-off mode $\mathcal{O}(10^{-7})$.
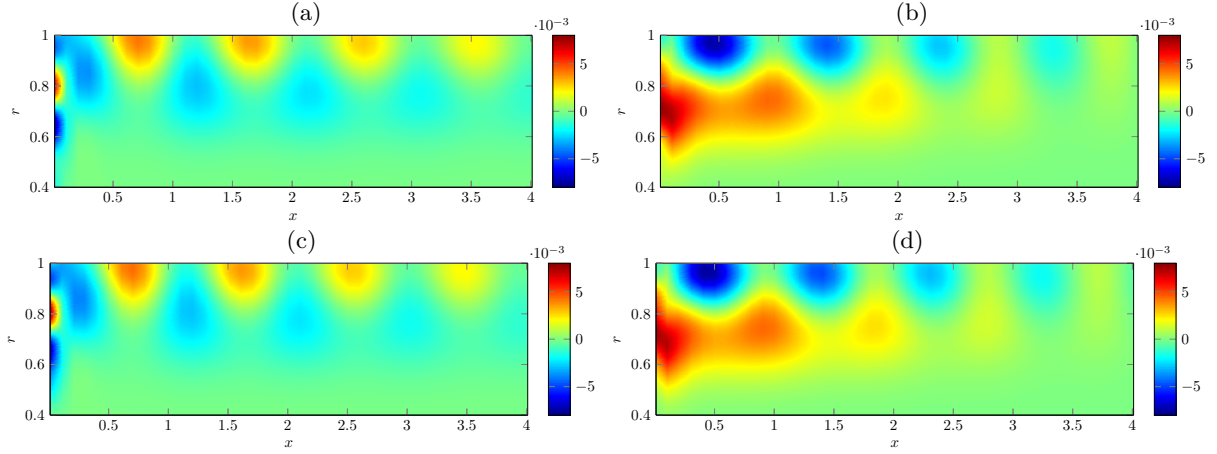
Figure 19: Colour plot of the acoustic Green's function $\widehat{p}_n^A(x, r | x_0, r_0)$ for a source at $(x_0, r_0) = (0, 0.8)$. (a) $\text{Re}(\widehat{p}_n^A)$ calculated asymptotically; (b) $\text{Im}(\widehat{p}_n^A)$ calculated asymptotically; (c) $\text{Re}(\widehat{p}_n^A)$ calculated numerically; (d) $\text{Im}(\widehat{p}_n^A)$ calculated numerically. The other parameters are $n = 8$, $\omega = 19.5$, $Z_j = 1 - 2\text{i}$ with mean flow profiles given in Figure 18.

5. Conclusions

In this paper we considered the eigenmodes and Green's function of the acoustic analogy in swirling flow from Posson and Peake [25]. We presented high-frequency asymptotics, which allowed us to calculate the eigenmodes and Green's function extremely accurately, even when we had lined walls and realistic mean swirling flow. When we have a more complicated mean flow profile (such as high order polynomials or realistic swirling flow) then the accuracy of the asymptotic method is reduced, although it still produces very accurate results. We also saw that the effect of swirl is very significant on the full Green's function, with Figures 7 and 8 showing the effect of swirl both asymptotically and numerically.

The only real challenge remaining is calculating the contribution from the critical layer, including the effect of the hydrodynamic modes, quickly and accurately.. The critical layer contribution comes from an integral around the critical layer and hydrodynamic modes, which is only present when considering the downstream Green's function. We ignored this contribution since, in general, it is small compared to the contribution from the cut-on acoustic modes [23]. Our asymptotic method is not very applicable to calculating the critical layer contribution, and the results were inaccurate (although of a similar order of magnitude) compared to the very expensive numerical calculation in the cases we tested. However, we believe that the hydrodynamic modes are of limited practical interest in most cases, but might be of a concern in isolated cases when the base flow is unstable.

As already noted, the Green's function calculated in this paper can be applied for noise prediction and mode detection analysis of test data, and work is proceeding on both issues.

Appendix A. Numerical eigenmodes

To calculate the eigenmodes numerically, we linearise the Euler equations, and only need to consider the momentum equations and a combined mass and energy equation due to the assumption of a homentropic fluid. These are given by

$$\frac{1}{c_0^2}\frac{D_0 p}{Dt} + \frac{\rho_0 U_\theta^2}{rc_0^2}v + \rho_0(\boldsymbol{\nabla}\cdot\boldsymbol{u}) = 0, \tag{A.1}$$

$$\rho_0\left(\frac{D_0 u}{Dt} + v\frac{dU_x}{dr}\right) + \frac{\partial p}{\partial x} = 0, \tag{A.2}$$

$$\rho_0\left(\frac{D_0 v}{Dt} - \frac{2U_\theta w}{r}\right) - \frac{U_\theta^2}{r}\rho + \frac{\partial p}{\partial r} = 0, \tag{A.3}$$

$$\rho_0\left(\frac{D_0 w}{Dt} + \frac{v}{r}\frac{d}{dr}(rU_\theta)\right) + \frac{1}{r}\frac{\partial p}{\partial \theta} = 0, \tag{A.4}$$

and we further use that for a homentropic fluid $\rho c_0^2 = p$. We then Fourier transform the flow variables in the axial and frequency domains, and take a Fourier series in the circumferential direction, with:

$$\{u,v,w,p\}(r,x,\theta,t) = \int \sum_n \int \{U(r),V(r),W(r),P(r)\}e^{ikx}dk\,e^{in\theta}e^{-i\omega t}d\omega. \tag{A.5}$$

We then solve the resulting eigenvalue problem for the axial wavenumber k. The final eigenvalue problem is given by (see Mathews [17] for the details)

$$-\frac{U_x\bar{\Omega}}{c_0^2\zeta}iU + \left[\frac{U_x}{c_0^2\zeta}\frac{dU_x}{dr} - \frac{1}{r\zeta} - \frac{U_\theta^2}{\zeta rc_0^2}\right]V - \frac{1}{\zeta}\frac{dV}{dr} - \frac{n}{r\zeta}iW + \frac{i\bar{\Omega}}{c_0^2\rho_0\zeta}P = kiU, \tag{A.6}$$

$$\frac{\bar{\Omega}}{U_x}V - \frac{2U_\theta}{rU_x}iW + \frac{i}{\rho_0 U_x}\frac{dP}{dr} - \frac{iU_\theta^2}{\rho_0 U_x rc_0^2}P = kV, \tag{A.7}$$

$$-\frac{1}{U_x}\left[\frac{U_\theta}{r} + \frac{dU_\theta}{dr}\right]V + \frac{\bar{\Omega}}{U_x}iW - \frac{in}{r\rho_0 U_x}P = kiW, \tag{A.8}$$

$$\frac{\rho_0\bar{\Omega}}{\zeta}U + i\frac{\rho_0}{\zeta}\left[\frac{dU_x}{dr} - \left(1 + \frac{U_\theta^2}{c_0^2}\right)\frac{U_x}{r}\right]V - \frac{i\rho_0 U_x}{\zeta}\frac{dV}{dr} + \frac{n\rho_0 U_x}{r\zeta}W - \frac{U_x\bar{\Omega}}{c_0^2\zeta}P = kP, \tag{A.9}$$

where

$$\bar{\Omega} = \omega - \frac{nU_\theta}{r} \text{ and } \zeta = 1 - \frac{U_x^2}{c_0^2}. \tag{A.10}$$

The boundary conditions for the eigenvalue problem are given by

$$Z_h\frac{\omega V(h)}{U_x(h)} + \frac{\bar{\Omega}(h)P(h)}{U_x(h)} - kP(h) = 0 \text{ and } Z_1\frac{\omega V(1)}{U_x(1)} - \frac{\bar{\Omega}(1)P(1)}{U_x(1)} + kP(1) = 0, \tag{A.11}$$

which follow from Fourier transforming the Myers boundary conditions in Eq. (6). We solve this eigenvalue problem using Chebfun in MATLAB [6], which avoids having to discretise the derivatives. To remove the eigenvalue from the boundary condition we either introduce a fifth variable $\bar{P} = kP$, or substitute Eq. (A.9) into the boundary conditions.

Our numerical eigenmode solver was validated against the results from the program in Posson and Peake [25]. We find that we get perfect agreement in all cases with Posson and Peake [25] once we have corrected a numerical implementation error in the lined boundary condition in Posson and Peake [25].

Appendix B. Numerical Green's function

The contribution from each acoustic eigenmode is given by

$$\widehat{p}_n^m(x, r | x_0, r_0) = \pm \frac{\mathrm{i}\omega}{4\pi^2} \mathrm{e}^{\mathrm{i}\omega\kappa_n^m(x - x_0)} \frac{1}{r_0 \frac{\partial \mathcal{W}}{\partial \kappa}(\kappa_n^m)} \begin{cases} g_1(r_0; \kappa_n^m) g_2(r; \kappa_n^m) & r \leq r_0 \\ g_2(r_0; \kappa_n^m) g_1(r; \kappa_n^m) & r > r_0 \end{cases}, \tag{B.1}$$

where we calculate $g_1(r; \kappa)$, $g_2(r; \kappa)$ and $\mathcal{W}(\kappa)$ numerically. We find $g_1(r; \kappa)$ and $g_2(r; \kappa)$ by solving the differential equation

$$\mathcal{A}(r, \kappa_n^m) \frac{\mathrm{d}^2 g_j}{\mathrm{d}r^2}(r; \kappa_n^m) + \mathcal{B}(r, \kappa_n^m) \frac{\mathrm{d}g_j}{\mathrm{d}r}(r; \kappa_n^m) - \mathcal{C}(r, \kappa_n^m) g_j(r; \kappa_n^m) = 0, \tag{B.2}$$

where

$$\mathcal{A}(r, \kappa) = (\mathcal{U}_\theta(r) - \omega^2 \Phi^2(r, \kappa)) \omega^2 \Phi^2(r, \kappa), \tag{B.3}$$

$$\mathcal{B}(r, \kappa) = \omega^2 \Phi^2(r, \kappa) \left[(\mathcal{U}_\theta(r) - \omega^2 \Phi^2(r, \kappa)) \left(\frac{1}{r} - \frac{\rho_0'(r)}{\rho_0(r)} \right) + \frac{\partial}{\partial r} (\omega^2 \Phi^2(r, \kappa) - \mathcal{U}_\theta(r)) \right], \tag{B.4}$$

and

$$\frac{\mathcal{C}(r, \kappa)}{\omega^2} = (\mathcal{U}_\theta - \omega^2 \Phi^2)^2 \left(\frac{\Phi^2}{c_0^2} - \kappa^2 - \frac{\eta^2}{r^2} \right) + \Upsilon^*(\mathcal{U}_\theta - \omega^2 \Phi^2) \left[\Upsilon^* + \Phi \left(\frac{1}{r} - \frac{\rho_0'}{\rho_0} \right) \right] \tag{B.5}$$
$$+ \Upsilon^*[\Phi(\omega^2 \Phi^2 - \mathcal{U}_\theta)]' - \Phi(\omega^2 \Phi^2 - \mathcal{U}_\theta)\Upsilon^{*\prime}.$$

The boundary conditions are given by

$$g_1(1; \kappa_n^m) = 1 \quad \text{and} \quad \frac{\mathrm{d}g_1}{\mathrm{d}r}(1; \kappa_n^m) = \widehat{f}_1(1, \kappa_n^m) g_1(1; \kappa_n^m), \tag{B.6}$$

and

$$g_2(h; \kappa_n^m) = 1 \quad \text{and} \quad \frac{\mathrm{d}g_2}{\mathrm{d}r}(h; \kappa_n^m) = \widehat{f}_2(h, \kappa_n^m) g_2(h; \kappa_n^m). \tag{B.7}$$

We can easily determine the functions $\widehat{f}_1(r, \kappa)$ and $\widehat{f}_2(r, \kappa)$ from Eq. (21) and Eq. (22), and they are related to the functions $f_j(r, \kappa)$ in Eq. (31). The choice of $g_1(1; \kappa_n^m) = 1$ and $g_2(h; \kappa_n^m) = 1$ is arbitrary, and was chosen for simplicity.

The difficulty in evaluating Eq. (B.1) lies in calculating the derivative of the Wrońskian with respect to κ. To calculate this we first find the derivatives of $g_1(r; \kappa)$ and $g_2(r; \kappa)$ with respect to κ, which we do by using the same method as Posson and Peake [25]. We differentiate Eq. (B.2) with respect to κ, which then gives

$$\mathcal{A}(r, \kappa_n^m) \frac{\mathrm{d}^2}{\mathrm{d}r^2} \left(\frac{\partial g_j}{\partial \kappa} \right) + \mathcal{B}(r, \kappa_n^m) \frac{\mathrm{d}}{\mathrm{d}r} \left(\frac{\partial g_j}{\partial \kappa} \right) - \mathcal{C}(r, \kappa_n^m) \frac{\partial g_j}{\partial \kappa} \tag{B.8}$$
$$= \frac{\partial \mathcal{C}}{\partial \kappa}(r, \kappa_n^m) g_j - \frac{\partial \mathcal{B}}{\partial \kappa}(r, \kappa_n^m) \frac{\mathrm{d}g_j}{\mathrm{d}r} - \frac{\partial \mathcal{A}}{\partial \kappa}(r, \kappa_n^m) \frac{\mathrm{d}^2 g_j}{\mathrm{d}r^2}.$$

Since we have already calculated $g_1(r; \kappa)$ and $g_2(r; \kappa)$, the right-hand side is known. We calculate the new boundary conditions by differentiating Eq. (B.6) and Eq. (B.7) with respect to κ, which gives

$$\frac{\partial g_1}{\partial \kappa}(1; \kappa_n^m) = 0 \quad \text{and} \quad \frac{\mathrm{d}}{\mathrm{d}r} \left(\frac{\partial g_1}{\partial \kappa} \right)(1; \kappa_n^m) = \frac{\partial \widehat{f}_1}{\partial \kappa}(1, \kappa_n^m) g_1(1; \kappa_n^m) + \widehat{f}_1(1, \kappa_n^m) \frac{\partial g_1}{\partial \kappa}(1; \kappa_n^m), \tag{B.9}$$

and

$$\frac{\partial g_2}{\partial \kappa}(h; \kappa_n^m) = 0 \quad \text{and} \quad \frac{\mathrm{d}}{\mathrm{d}r} \left(\frac{\partial g_2}{\partial \kappa} \right)(h; \kappa_n^m) = \frac{\partial \widehat{f}_2}{\partial \kappa}(h, \kappa_n^m) g_2(h; \kappa_n^m) + \widehat{f}_2(h, \kappa_n^m) \frac{\partial g_2}{\partial \kappa}(h; \kappa_n^m). \tag{B.10}$$

25

We then solve Eq. (B.8) with the boundary conditions in Eq. (B.9) to calculate $\partial g_1/\partial\kappa$, and Eq. (B.8) with the boundary conditions in Eq. (B.10) to calculate $\partial g_2/\partial\kappa$. Finally, the derivative of the Wrońskian is given by

$$\frac{\partial\mathcal{W}}{\partial\kappa} = \frac{\partial g_1}{\partial\kappa}\frac{\mathrm{d}g_2}{\mathrm{d}r} + g_1\frac{\mathrm{d}}{\mathrm{d}r}\left(\frac{\partial g_2}{\partial\kappa}\right) - g_2\frac{\mathrm{d}}{\mathrm{d}r}\left(\frac{\partial g_1}{\partial\kappa}\right) - \frac{\partial g_2}{\partial\kappa}\frac{\mathrm{d}g_1}{\mathrm{d}r}, \tag{B.11}$$

which is straightforward to calculate now, since derivatives with respect to r are easy to calculate numerically. The Green's function results were validated by comparing with the results in [25], with exact agreement in all cases once we have corrected the numerical implementation error in the lined boundary condition in [25].

References

[1] C. M. Bender and S. A. Orszag. *Advanced mathematical methods for scientists and engineers I: Asymptotic methods and perturbation theory*. Springer, 1978.

[2] W. E. Boyce, R. C. DiPrima, and C. W. Haines. *Elementary differential equations and boundary value problems*. Wiley New York, 7th edition, 1992.

[3] A. J. Cooper and N. Peake. Propagation of unsteady disturbances in a slowly varying duct with mean swirling flow. *Journal of Fluid Mechanics*, 445:207–234, 2001.

[4] A. J. Cooper and N. Peake. Upstream-radiated rotor–stator interaction noise in mean swirling flow. *Journal of Fluid Mechanics*, 523:219–250, 2005.

[5] N. Curle. The influence of solid boundaries upon aerodynamic sound. In *Proceedings of the Royal Society of London A: Mathematical, Physical and Engineering Sciences*, volume 231, pages 505–514. The Royal Society, 1955.

[6] T. A. Driscoll, N. Hale, and L. N. Trefethen. *Chebfun Guide*. Pafnuty Publications, Oxford, 2014.

[7] D. G. Duffy. *Green's functions with applications*. CRC Press, 2001.

[8] J. E. Ffowcs Williams and D. L. Hawkings. Sound generation by turbulence and surfaces in arbitrary motion. *Philosophical Transactions of the Royal Society of London. Series A, Mathematical and Physical Sciences*, 264(1151):321–342, 1969.

[9] M. E. Goldstein. An exact form of Lilley's equation with a velocity quadrupole/temperature dipole source term. *Journal of Fluid Mechanics*, 443:231–236, 2001.

[10] V. V. Golubev and H. M. Atassi. Acoustic–vorticity waves in swirling flows. *Journal of Sound and Vibration*, 209:203–222, 1998.

[11] C. J. Heaton and N. Peake. Acoustic scattering in a duct with mean swirling flow. *Journal of Fluid Mechanics*, 540: 189–220, 2005.

[12] C. J. Heaton and N. Peake. Algebraic and exponential instability of inviscid swirling flow. *Journal of Fluid Mechanics*, 565:279–318, 2006.

[13] R. E. Langer. On the asymptotic solutions of ordinary differential equations, with reference to the Stokes' phenomenon about a singular point. *Transactions of the American Mathematical Society*, 37(3):397–416, 1935.

[14] M. J. Lighthill. On sound generated aerodynamically. I. General theory. In *Proceedings of the Royal Society of London A: Mathematical, Physical and Engineering Sciences*, volume 211, pages 564–587. The Royal Society, 1952.

[15] G. M. Lilley. On the noise from jets. *AGARD Technical Report CP-131*, pages 13.1–13.12, 1974.

[16] V. Masson, H. Posson, M. Sanjose, S. Moreau, and M. Roger. Fan-OGV interaction broadband noise prediction in a rigid annular duct with swirling and sheared mean flow. In *22nd AIAA/CEAS Aeroacoustics Conference, Lyon*, 2016.

[17] J. R. Mathews. *Mathematical modelling of noise generation in turbofan aeroengines using Green's functions*. PhD thesis, University of Cambridge, 2016.

[18] J. R. Mathews, N. Peake, and S. Bianchi. Asymptotic and numerical Green's function in a lined duct with realistic shear and swirl. In *22nd AIAA/CEAS Aeroacoustics Conference, Lyon*, 2016.

[19] C. L. Morfey and M. C. M. Wright. Extensions of Lighthill's acoustic analogy with application to computational aeroacoustics. In *Proceedings of the Royal Society of London A: Mathematical, Physical and Engineering Sciences*, volume 463, pages 2101–2127. The Royal Society, 2007.

[20] M. K. Myers. On the acoustic boundary condition in the presence of flow. *Journal of Sound and Vibration*, 71(3):429–434, 1980.

[21] R. B. Nielsen and N. Peake. Tunnelling effects for acoustic waves in slowly varying axisymmetric flow ducts. *Journal of Sound and Vibration*, 380:180–191, 2016.

[22] N. Peake and A. B. Parry. Modern challenges facing turbomachinery aeroacoustics. *Annual Review of Fluid Mechanics*, 44:227–248, 2012.

[23] H. Posson and N. Peake. Acoustic analogy in swirling mean flow applied to predict rotor trailing-edge noise. In *18th AIAA/CEAS Aeroacoustics Conference, Colorado Springs*, 2012.

[24] H. Posson and N. Peake. Swirling mean flow effect on fan-trailing edge broadband noise in a lined annular duct. In *19th AIAA/CEAS Aeroacoustics Conference, Berlin*, 2013.

[25] H. Posson and N. Peake. The acoustic analogy in an annular duct with swirling mean flow. *Journal of Fluid Mechanics*, 726:439–475, 2013.

[26] D. C. Pridmore-Brown. Sound propagation in a fluid flowing through an attenuating duct. *The Journal of the Acoustical Society of America*, 30(7):670–670, 1958.

[27] S. W. Rienstra. Sound transmission in slowly varying circular and annular lined ducts with flow. *Journal of Fluid Mechanics*, 380:279–296, 1999.

[28] S. W. Rienstra and B. J. Tester. An analytic Green's function for a lined circular duct containing uniform mean flow. *Journal of Sound and Vibration*, 317(3):994–1016, 2008.

[29] Sjoerd W Rienstra. Fundamentals of duct acoustics. *Von Karman Institute Lecture Notes*, 2015.

[30] P. Sijtsma. Using phased array beamforming to locate broadband noise sources inside a turbofan engine. In *AARC Engine Noise Phased Array Workshop, Cambridge (MA)*, 2006.

[31] P. Sijtsma. Green's functions for in-duct beamforming applications. In *18th AIAA/CEAS Aeroacoustics Conference, Colorado Springs*, 2012.

[32] C. K. W. Tam and L. Auriault. The wave modes in ducted swirling flows. *Journal of Fluid Mechanics*, 371:1–20, 1998.

[33] G. G. Vilenski and S. W. Rienstra. On hydrodynamic and acoustic modes in a ducted shear flow with wall lining. *Journal of Fluid Mechanics*, 583:45–70, 2007.

[34] G. G Vilenski and S. W. Rienstra. Numerical study of acoustic modes in ducted shear flow. *Journal of Sound and Vibration*, 307(3):610–626, 2007.

[35] D. W. Wundrow and A. Khavaran. On the applicability of high-frequency approximations to Lilley's equation. *Journal of Sound and Vibration*, 272(3):793–830, 2004.